Modelling electromechanical transduction at finite deformation.

Treball realitzat per:
Nikhil Dave

Dirigit per:
Prof. Irene Arias
Prof. Amir Abdollahi

Màster en:
Erasmus Mundus MSc. Computational Mechanics

Barcelona, **July 05 2018**

Department of Civil & Environmental Engineering

TREBALL FINAL DE MÀSTER

UNIVERSITAT POLÌTECNICA DE CATALUNYA

MASTERS THESIS

Modelling electromechanical transduction at finite deformation

---

Author:
Nikhil Dave

Supervisors:
Prof. Irene Arias &
Prof. Amir Abdollahi

An Industrial Project report submitted in fulfilment of the requirements for the degree of
Master of Science in Computational Mechanics

at

Centre Internacional de Mètodes Numèrics a l'Enginyeria (CIMNE)
Universitat Polìtecnica de Catalunya

July 2018

Declaration

I, Nikhil Dave, declare that this Master thesis titled, 'Modelling electromechanical transduction at finite deformation' and the work presented in this report are my own. This project report is about developing a finite element method model to capture the electromechanical behaviour of a dielectric elastomeric film sandwiched between the two compliant electrodes. The research has been conducted upon completion of my two years of the MSc. program in Computational Mechanics at Swansea University and Universitat Polìtecnica de Catalunya (UPC). The place of research was Laboratori de Càlcul Numèric - LaCàN, UPC. I confirm that:

- this work was done wholly in candidature for a masters degree at Swansea University and Universitat Polìtecnica de Catalunya (UPC).

- the research was carried out at Laboratori de Càlcul Numèric - LaCàN, UPC, Barcelona, Spain.

- wherever previously published work of others has been included in this report, it has always been attributed.

- acknowledgements of all the sources which have helped me in the compilation of this report have been done.

Signed: *N. Dave*

Date: *05.07.2018*

Abstract

The purpose of this study is to understand the basic principle of electromechanical transduction in electroactive polymers. These active materials have intrinsic nature to respond to external stimulus and alter their properties making them very attractive for applications in actuators, sensors, artificial muscles, lifelong batteries, etc.

In this research work, the nonlinear electroelasticity framework is used to exploit the large deformation capacity of dielectric elastomeric actuators. The fundamental constituents required for the formulation and computation of nonlinear electroelastic problems are provided in this report.

The variational formulation and the finite element method used to solve the nonlinear electromechanical transduction problem are explained and the later is implemented using MATLAB. The code is validated for a benchmark problem where contraction in a long cylinder is observed under the application of electric potential across its thickness. Both compressible and nearly incompressible dielectric elastomeric films are also analysed with the implemented code.

The surface instabilities associated with dielectric elastomers under the application of surface tension are studied. The creasing to wrinkling transition observed experimentally is well captured in the simulations.

Keywords: Electromechanical transduction, Dielectric elastomer actuator, Numerical Modelling, Finite Element Method, Hyperelasticity, MATLAB

Acknowledgements

Contents

List of Figures

List of Tables

Abbreviations

EAP	**E**lectro **A**ctive **P**olymer
PZT	Lead **Z**irconate **T**itanate
DE	**D**ielectric **E**lastomer
DEA	**D**ielectric **E**lastomer **A**ctuator
FEM	**F**inite **E**lement **M**ethod
BVP	**B**oundary **V**alue **P**roblem
GIS	**G**rid **I**ndependence **S**tudy
SMA	**S**hape **M**emory **A**lloys
MPE	**M**inimum **P**otential **E**nergy
2D	**2** **D**imensional
3D	**3** **D**imensional

Nomenclature

<u>Vectors</u>

$\boldsymbol{X}$	Particle position in material description
$\boldsymbol{E_I}$	Cartesian basis in material description
$\boldsymbol{x}$	Particle position in spatial description
$\boldsymbol{e_i}$	Cartesian basis in spatial description
$d\boldsymbol{X}$	Relative material position of two adjacent particles
$d\boldsymbol{x}$	Relative spatial position of two adjacent particles
$\boldsymbol{F}$	Deformation gradient tensor
$\boldsymbol{C}$	Right Cauchy-Green deformation tensor
$\boldsymbol{\sigma}_e$	Maxwell stress
$\boldsymbol{\sigma}_{el}$	Electrostrictive stress
$\boldsymbol{D}$	Electric displacement vector vector in material configuration
$\boldsymbol{d}$	Electric displacement vector in spatial configuration
$\boldsymbol{E}$	Electric field vector in material configuration
$\boldsymbol{e}$	Electric field vector in spatial configuration
$\boldsymbol{P}$	Electric polarization density in material configuration
$\boldsymbol{p}$	Electric polarization density in spatial configuration
$\boldsymbol{\varphi}$	Electric potential vector
$\boldsymbol{\chi}$	Displacement vector
$\boldsymbol{\sigma}$	Cauchy stress tensor
$\boldsymbol{f}_e$	Electric body force
$\boldsymbol{T}$	Total nominal stress tensor in material configuration
$\boldsymbol{\tau}$	Total stress tensor in spatial configuration

$\boldsymbol{\varepsilon}$ Permutation tensor

$\boldsymbol{N}$ Unit normal to the surface

$\overline{\boldsymbol{T}}$ External traction vector

$\boldsymbol{K}_{surf}$ Stiffness due to surface tension

$\boldsymbol{f}_{surf}$ Surface forces due to surface tension

Latin Characters

V Voltage

H Thickness of the elastomer

t Time

J Jacobian

dv Volume element in spatial configuration

dV Volume element in material configuration

W Total potential enenrgy

W_{int} Internal energy density per referential unit volume

W_{ext} External energy density per referential unit volume

$\overline{Q}$ External electric charge

L_e Length of the face of an element

h Out-of-plane thickness

Greek Characters

ϵ_0 Free space permittivity

ϵ_r Relative permittivity

Ψ Strain energy density function

ϕ Electric potential in material configuration

φ Electric potential in spatial configuration

Ω_0 Body in material configuration

Ω	Body in spatial configuration
$\partial\Omega_0$	Boundary of the body in material configuration
$\partial\Omega$	Boundary of the body in spatial configuration
$\partial\Omega_{0_\tau}$	Boundary of the body in spatial configuration with external electric charge
$\partial\Omega_{0_q}$	Boundary of the body in spatial configuration with external electric charge
Φ	Mapping
μ	Shear modulus
κ	Bulk modulus
λ	Lamé first parameter
γ	Surface tension

Superscripts

For any arbitrary quantity 'Q' the superscript denotes the value of Q:

Q^T	after taking a transpose
Q^e	at the elemental domain

Operators

$\nabla()$	Gradient
$\nabla \cdot ()$	Divergence
$\nabla \times ()$	Curl
$\otimes$	Cross product
:	Inner product
$\frac{\partial()}{\partial t}$	Partial Derivative
$\frac{d()}{dt}$	Local Derivative

Chapter 1

Introduction

1.1 Background and Motivation

1.1.1 Smart materials

With everyday advances in technology and shrinking electronics, there is a tremendous interest among innovators and consumers in self-powered, compact, wearable and implantable smart devices which have an inherent nature to significantly alter [5] their properties in response to an external stimulus like temperature, light, electric and magnetic fields.
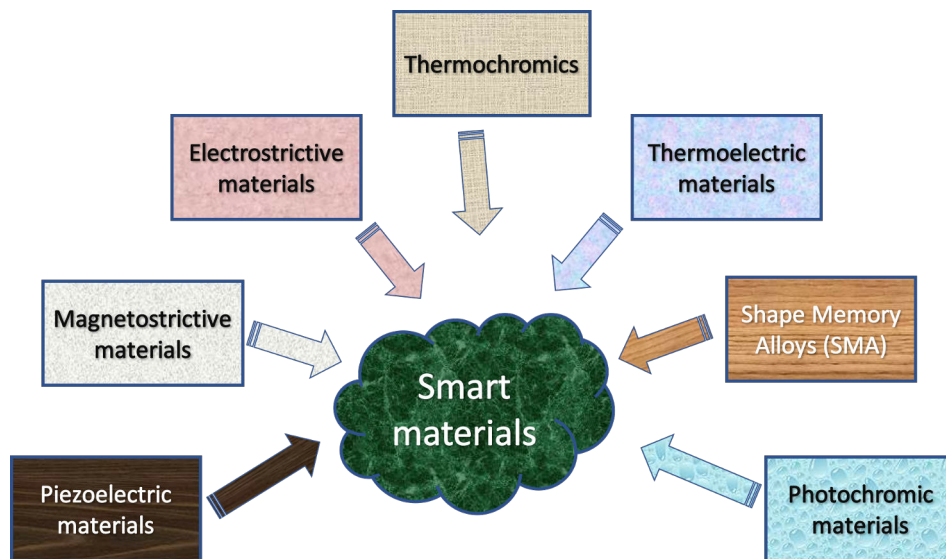
FIGURE 1.1: Types of smart materials.

This research work essentially revolves around smart materials, their properties and applications. The ability of these active materials to respond to external stimulus makes them highly attractive for applications in actuators, sensors and energy harvesting devices [1]. Figure 1.1 shows some of the commonly known types of the smart materials.

Despite extensive research in energy harvesting, fossil fuel remains the primary and traditional source of energy, which is not only non-renewable but also raises severe environmental concerns. Ambient energy scavenging addresses these issues, making smart materials an ideal choice to reduces the dependence on batteries [7].

Smart materials can be classified as per their input and output energy source [2]. Table 1.1 shows a few smart materials classified as per their inherent transduction properties.

Type of Smart materials	Input	Output
Piezoelectric	Potential difference	Deformation
Electrostrictive	Potential difference	Deformation
Magnetostrictive	Magnetic field	Deformation
Thermoelectric	Temperature	Potential difference
Shape Memory Alloys	Temperature	Deformation
Photochromic	Radiation	Colour change
Thermochromics	Temperature	Colour change

TABLE 1.1: Classification of Smart materials.

Piezoelectric materials are gaining popularity among researchers due to their ability to emulate biological operations like artificial muscles and variety of applications in actuators, sensors, energy harvesters and life-long batteries. Piezoelectric materials undergo mechanical change when subjected to variation in electric potential or voltage and generate usable electrical energy when subjected to mechanical stress. These effects are known as the direct and converse effects.

Historically, one of the most commonly researched smart materials is the ceramic piezoelectric materials, notably, lead zirconate titanate (PZT) [8] [7]. However, these materials are associated with producing small strains for an applied electric field, are brittle in nature and contain lead−raising environmental concerns.

With the world moving towards lead-free energy sources for environment protection, extensive research has been conducted on developing lead-free alternatives with matching or even better properties than lead zirconate titanate (PZT).

A number of smart materials have seen a fair amount of use in actuators like magnetostrictive materials and Shape Memory Alloys (SMA), which provide large deformations at the cost of application of magnetic field and temperature change, respectively.

In the past few decades, a lot of interest has grown in Electroactive polymers (EAP) materials due to their capacity to exhibit up to 380% strain [5], which is much higher than in a ceramic actuator and thus has the potential to become a lead-free alternative. The work of Dorfmann & Ogden [3] in nonlinear theory of electroelastic and magnetoelastic interactions is well motivated towards development of elastomeric materials capable of large deformations by application of an electric or magnetic field.

1.1.2 Electroactive polymers (EAP)

Electroactive polymers (EAP) are dielectric soft materials that can transform electric energy into mechanical work by producing sizeable strains in response to an electrical stimulus. Due to their ability to sustain high forces and undergo large deformation, they are actively being used as actuators and sensors. EAPs are often called 'artificial muscles' due to their capability to impersonate biological muscles [5].

EAPs can be classified as Ionic EAPs [20] [21] and Electric EAPs [23] [22], where the former is driven by the movement of ions and in the latter strong electric field drives the actuation. Only a few volts are needed for actuation in Ionic EAPs whereas Electric EAPs need high voltages (hundreds to thousands of volts) to be activated. A few examples of ionic EAPs are the Polyelectrolyte gels and carbon nanotubes while the electric EAPs have two main electromechanical coupling mechanisms - piezoelectricity possessed by piezoelectric polymers and electrostriction which is present in all dielectric polymers or dielectric elastomers.

1.1.3 Dielectric Elastomers (DE)

Dielectric elastomers (DE) are incompressible dielectrics, belonging to electric EAPs, which undergo large deformations in response to applied electric fields. The use of these materials [24] in

specific applications like actuators is found essentially due to their ability to undergo finite deformation, high-speed response (attributing to strong electromechanical coupling), lightweight nature and better efficiency than devices based on conventional technologies [22] [23]. For application in actuators, these materials are primarily used as thin films covered with compliant electrodes on either sides and stacked together to form multilayers. Experimental research in dielectric elastomers began with the seminal work of Pelrine et al. about two decades ago [23] [22] and since then there have been many experimental ([24] [17] [14] [19]), theoretical ([9] [3] [18]) and a few computational ([13] [12] [26] [4]) research work.

1.1.4 Dielectric Elastomeric Actuators (DEA)

The use of soft materials in actuator application has been a promising research field over the years ([22] [23] [24] [25] [9] [13] [17]). A Dielectric Elastomer Actuator (DEA) consists of incompressible elastomeric films [23], behaving as capacitors, that are sandwiched between two compliant electrodes as shown in Figure 1.2.
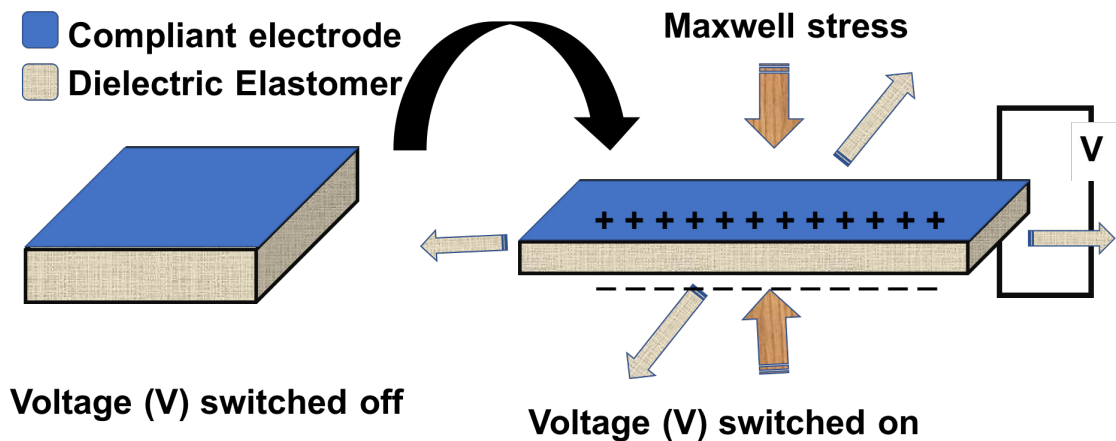
FIGURE 1.2: Behaviour of a DEA on application of electric potential (V) [10].

There are two sources of strains in a Dielectric Elastomeric Actuator (DEA) [24]. Firstly, the application of electric field generates Coulomb forces between the electrodes due to the appearance of positive charges on one electrode and negative charges on the other. For an applied voltage, V, between the electrodes, these forces generate a pressure, $\boldsymbol{\sigma}_e$, between the electrodes known as Maxwell stresses [23] [22]. This effect is present always in a dielectric.

Although in hard materials (e.g. ceramics) the induced strain is negligible but not in soft materials (polymers). The Maxwell stress induced is given by,

$$\boldsymbol{\sigma}_e = \epsilon_r \epsilon_0 \Big(\frac{V}{H}\Big)^2 \tag{1.1}$$

where ϵ_r and ϵ_0 are the elastomer relative permittivity and free space permittivity, respectively and H is the thickness of the elastomer.

The second source is known as electrostriction and is related to change in properties of the dielectric with electric potential. All dielectrics have a property to vary the dielectric constant with strain. It has been reported in the experimental literature that the electric permittivity of dielectric elastomers (dielectric constant) is a function of the deformation gradient [25]. This change in dielectric constant gives rise to deformation due to electrostriction. This effect can be mathematically written as,

$$\boldsymbol{\sigma}_{el} = \epsilon_r \epsilon_0 \Big(\frac{V}{H}\Big)^2 \Big(1 - \frac{a_1}{2\epsilon_r}\Big) \tag{1.2}$$

which essentially is the same as the Maxwell stress and an additional term with electrostrictive coefficient a_1 which shows the change in dielectric properties of the material. Most of the polymers display a relatively low degree of electrostriction due to low dielectric permittivity values which has been experimentally shown by G. Kofod et al. [24].

Both the effects are quadratic in nature and act by contracting the dielectric elastomer in the direction of the Coulomb forces [9] [24]. The incompressible nature of a dielectric elastomeric actuator makes it expand in the perpendicular direction. Therefore, it is important for the electrodes to behave as compliant layers and provide the least resistance to the deformation.

Since the strain generated by a dielectric elastomer actuator is proportional to both the square of the applied voltage and the material dielectric constant (elastomer relative permittivity), utilising the inherent softness and compliance of these elastomers, a higher permittivity can be advantageously employed at lower voltages to drive these actuators.

1.2   Research Objectives

The main objective of the research is to model and simulate the actuator applications of dielectric elastomers and analyse the deformation as a function of applied voltage. To account for finite deformations, we need to utilise the theory of nonlinear continuum mechanics.

In order to model the dielectric elastomer material, a constitutive model describing incompressible nonlinearly elastic material response is also required to be coupled with Maxwell stress effect. A better understanding of this coupling phenomenon is one of the main objectives of this research work.

Numerical modelling is needed to solve the above mathematical formulations and simulate the real behaviour of an actuator. The use of the implementation in solving boundary value problems and also studying the instabilities associated with modelling dielectric elastomeric actuators is an important part of this research work.

Lastly, validating our implementation by comparing the the obtained simulation results with the previously published work in the area of dielectric elastomer actuators is vital in checking the usefulness and correctness of the results obtained.

1.3   Outline

The work presented in this report is divided into eight chapters. In Chapter 1 we look at the dielectric smart materials—its general introduction, properties and future applications. To gain insight into the modelling of dielectric elastomer actuator, a literature study was conducted and is documented in Chapter 1 with sections concentrating on the research objectives, the scope of the project, the approach and tools used in the analysis. The outline of the research report is also presented.

Chapter 2 offers a short theoretical background. The basics of nonlinear continuum mechanics theory are outlined and the details of the considered hyperelastic material models are presented. In addition to the constitutive model and strain energy potential formulation, the electromechanical coupling formulation is also explained.

Chapter 3 contains the numerical implementation of the constitutive model and electromechanical coupling. A nonlinear finite element program is developed for numerical calculations of the electromechanical problem with different constitutive models.

In Chapter 4, the numerical model developed in Chapter 3 is used to apply voltage iteratively as an input while recording the time history of the strains as an output. A short review of the pre-processing tool used, GiD, is also presented in this chapter.

The simulation results for a long cylindrical actuator and a dielectric elastomer film are then presented followed by a Grid Independence Study (GIS) to determine the optimal mesh size in the analysis. Finally, the results are validated with the published research work on nonlinear electroelasticity, which serves as a verification of our implementation using finite element method.

In Chapter 5, we implement and simulate a thin nearly-incompressible dielectric elastomeric film and analyse the obtained deformation results with incorporation of a few other concepts like surface tension.

We also study the instabilities associated with modelling dielectric elastomer actuators due to the presence of surface tension on the surface of the film. The surface tension or elastocapillary number is used to determine the transition of surface creasing and wrinkling on the dielectric elastomer surface and resistance to contraction.

Finally, in Chapter 6, the most important findings of this work are highlighted and some recommendations are given for the future research.

1.4 General Remarks

- All properties are expressed in SI units specified in the 'Nomenclature' unless otherwise stated.
- Vectors and tensors are represented by ***bold*** characters.

Chapter 2

Basic Theory and Models

This chapter gives a theoretical background of the mechanical behaviour of dielectric elastomer actuators under electrical loading and their electromechanical coupling formulation. Since it is essential to have a good understanding of the theory and assumptions in the numerical study, the basic ingredients of nonlinear continuum mechanics are presented first, followed by the electromechanical constitutive model. Further elaboration and detailed derivations can be found in the literature suggested.

2.1   Nonlinear Continuum Mechanics

Constitutive models are the mathematical description of the relationship between two physical quantities (generally kinetic and kinematic quantities) for a particular material. It is basically an approximation of how a material responds to an external loading [11].

Due to their multi-physics behaviour, the constitutive models for smart materials couples their mechanical response with other physical fields e.g. electromechanical transduction where electrostatic energy is transformed into mechanical energy or vice versa. This direct and reverse effect can be seen in piezoelectric materials to be utilised in actuators or sensors applications. [4]

However, in dielectric elastomers the ability to sense is limited to only piezoresistivity where a change only in the electrical resistivity, not in electric potential, of the material can be noticed on the application of mechanical strain. This is also known as electrostriction.

Dielectric elastomer materials are usually modelled as incompressible hyperelastic materials due to their homogeneous and isotropic nature and the ability to undergo finite deformations.

The theoretical framework of the nonlinear continuum mechanics provided in this chapter aims to capture the incompressible and large strain behaviour of a material.

2.1.1 Kinematics

We consider a general motion of deformable body [11], with its reference configuration Ω_0 and current configuration Ω, as shown in Figure 2.1. The consideration of finite deformation allows us to operate on distinct coordinate systems—material and spatial descriptions—associated with the names Lagrange and Euler, respectively.
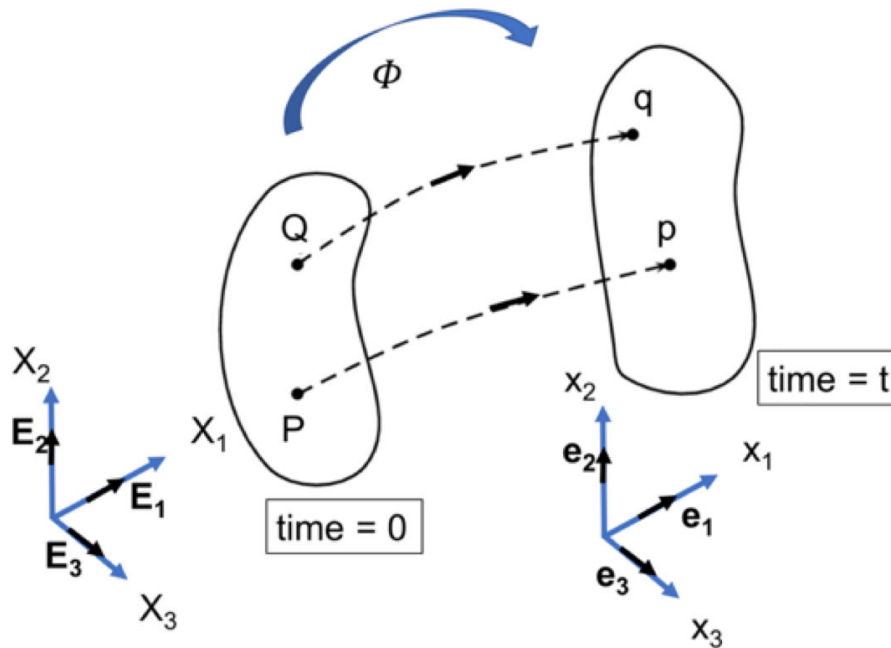
FIGURE 2.1: General motion of deformable body [11].

The position of the particles in the material (reference) description is given by coordinates $\boldsymbol{X}$ with respect to cartesian basis $\boldsymbol{E}_I$ and is independent of time while the particle's position in the spatial (current) description is given by coordinates $\boldsymbol{x}$ with respect to cartesian basis $\boldsymbol{e}_i$ at time t. The boundary of the body in the material and spatial configuration are given by $\partial\Omega_0$ and $\partial\Omega$, respectively.

The mathematical description of motion with time between the reference and current particle positions is given by a mapping Φ as,

$$\boldsymbol{x} = \Phi(\boldsymbol{X}, t) \tag{2.1}$$

The deformation of the body, shown in Figure 2.1, is described as the relative position of two adjacent particles after deformation, $d\boldsymbol{x}$, in terms of their relative material position, $d\boldsymbol{X}$, by the deformation gradient tensor, $\boldsymbol{F}$ as

$$\boldsymbol{F} = \frac{\partial \boldsymbol{x}}{\partial \boldsymbol{X}} \tag{2.2}$$

In indical notation, it is defined as [11],

$$\boldsymbol{F} = \sum_{i,I=1}^{3} F_{iI} \boldsymbol{e}_i \otimes \boldsymbol{E}_I; \quad F_{iI} = \frac{\partial x_i}{\partial X_I}; \quad i, I = 1, 2, 3 \tag{2.3}$$

where lowercase indices refer to current (spatial) Cartesian coordinates and uppercase indices refer to initial (material) Cartesian coordinates. This is because $\boldsymbol{F}$ is a two-point tensor which transforms vectors in the initial configuration into vectors in the current configration.

The spatial scalar product $d\boldsymbol{x}_1 \cdot d\boldsymbol{x}_2$ in terms of the material vectors $d\boldsymbol{X}_1$ and $d\boldsymbol{X}_2$ can be expressed as,

$$d\boldsymbol{x}_1 \cdot d\boldsymbol{x}_2 = (\boldsymbol{F} \, d\boldsymbol{X}_1) \cdot (\boldsymbol{F} \, d\boldsymbol{X}_2) = d\boldsymbol{X}_1 \cdot (\boldsymbol{F}^T \boldsymbol{F}) \boldsymbol{X}_2 = \boldsymbol{X}_1 \cdot \boldsymbol{C} \boldsymbol{X}_2 \tag{2.4}$$

where $\boldsymbol{C}$ is the right Cauchy-Green deformation tensor given as,

$$\boldsymbol{C} = \boldsymbol{F}^T \boldsymbol{F}; \quad \boldsymbol{C} = \sum_{I,J=1}^{3} C_{IJ} \boldsymbol{E}_I \otimes \boldsymbol{E}_J \tag{2.5}$$

As $\boldsymbol{C}$ operates on the material tensors $d\boldsymbol{X}_1$, $d\boldsymbol{X}_2$ and is consequently a material tensor.

The determinant of the deformation gradient tensor, $\boldsymbol{F}$, is a measure of distortion of the body and is referred to as the Jacobian J. The Jacobian is given as a measure of volume change by

defining it as the ratio between a volume element in the current configuration, dv, and reference configuration, dV, as [11],

$$J = \det(\boldsymbol{F}) = \frac{dv}{dV} \tag{2.6}$$

It is easily seen that for an incompressible material the Jacobian is equal to 1.

2.1.2 Hyperelectroelasticity

The nonlinear theory of elasticity requires a proper description of the stress-strain relation, incompressible behaviour and finite deformation. For this purpose we consider a strain energy density function, Ψ [12] given as,

$$\Psi(\boldsymbol{F}, \boldsymbol{E}) = \psi(\boldsymbol{F}, \boldsymbol{E}) + c_1 \boldsymbol{I} : [\boldsymbol{E} \otimes \boldsymbol{E}] + c_2 \boldsymbol{C} : [\boldsymbol{E} \otimes \boldsymbol{E}] \\ - \frac{1}{2}\varepsilon_0 J \boldsymbol{C}^{-1} : [\boldsymbol{E} \otimes \boldsymbol{E}] \tag{2.7}$$

where ψ represents a hyperelastic energy function in absence of electric field, c_1 and c_2 are the material constants and the terms $\boldsymbol{I} : [\boldsymbol{E} \otimes \boldsymbol{E}]$ and $\boldsymbol{C} : [\boldsymbol{E} \otimes \boldsymbol{E}]$ show the electrostatic and nonlinear coupling behaviour. ε_0 is the vacuum permittivity.

For an isotropic material, the strain energy density function, Ψ must be a function of six invariants [12] of right Cauchy-Green tensor, $\boldsymbol{C}$, and of $\boldsymbol{E} \otimes \boldsymbol{E}$, which are,

$$I_1 = \boldsymbol{C} : \boldsymbol{I}; \quad I_2 = \boldsymbol{C} : \boldsymbol{C}; \quad I_3 = \det \boldsymbol{C}; \\ I_4 = \boldsymbol{I} : (\boldsymbol{E} \otimes \boldsymbol{E}); \quad I_5 = \boldsymbol{C} : (\boldsymbol{E} \otimes \boldsymbol{E}); \quad I_6 = \boldsymbol{C}^2 : (\boldsymbol{E} \otimes \boldsymbol{E}) \tag{2.8}$$

In a hyperelastic constitutive model, the strain energy density function, Ψ, is utilised to define the nonlinear stress-strain behaviour of the material [11]. The mathematical description defined by specifying the dependence of strain energy density function, $\Psi(\boldsymbol{F}, \boldsymbol{E})$ on the deformation gradient, $\boldsymbol{F}$ and electric field vector, $\boldsymbol{E}$ in the reference configuration. This dependence is useful in computing the total nominal stress tensor and electric displacement vector by,

$$\boldsymbol{T} = [\partial_{\boldsymbol{F}}\Psi]^T; \quad \boldsymbol{D} = -\partial_{\boldsymbol{E}}\Psi \tag{2.9}$$

Several strain energy potential functions are available for describing the material model like Neo-Hookean [12], Mooney-Rivlin [11], Ogden [3], Arruda-Boyce [13] [17]. In the current work, we have used the Neo-Hookean and Arruda-Boyce models.

For the Neo-Hookean like material, we considered a strain energy density function [11] [13] [12] given as,

$$\Psi = \frac{\mu}{2}[\boldsymbol{C} : \boldsymbol{I} - 3] - \mu \ln J + \frac{\lambda}{2}[\ln J]^2 + c_1 \boldsymbol{I} : [\boldsymbol{E} \otimes \boldsymbol{E}] + c_2 \boldsymbol{C} : [\boldsymbol{E} \otimes \boldsymbol{E}] \\ - \frac{1}{2}\varepsilon_0 J \boldsymbol{C}^{-1} : [\boldsymbol{E} \otimes \boldsymbol{E}] \tag{2.10}$$

where the Lame parameters, μ and λ, determine the elastic behaviour.

The considered energy function behaves as a Neo-Hookean type in the absence of electric field and since we are interested in finite deformation problems, taking the small value of vacuum permittivity, $\varepsilon_0 (\approx 8.8542 \times 10^{-12} C^2 N^{-1} m^{-2})$, into account, we neglect the contribution of free space term $(1/2\varepsilon_0 \boldsymbol{C}^{-1} : [\boldsymbol{E} \otimes \boldsymbol{E}])$ in the energy formulation.

It has been validated by Wissler and Mazza [17] that Arruda-Boyce model is accurate for modelling large deformations in dielectric elastomers. Therefore, in this analysis, we also used the Arruda-Boyce strain energy density function [13] to model the mechanical behaviour of the dielectric elastomer. It is given as,

$$\Psi(\boldsymbol{C}, \boldsymbol{E}) = \mu \Psi_0 - 2\mu \Psi_0 \ln J - \frac{\lambda}{2}[\ln J]^2 + c_1 \boldsymbol{I} : [\boldsymbol{E} \otimes \boldsymbol{E}] + c_2 \boldsymbol{C} : [\boldsymbol{E} \otimes \boldsymbol{E}] \tag{2.11}$$

where we neglect the contribution of free space term $(1/2\varepsilon_0 \boldsymbol{C}^{-1} : [\boldsymbol{E} \otimes \boldsymbol{E}])$ and the mechanical free energy, Ψ_0 is approximated by a truncated series expansion, with N giving a measurement of the cross link density, as,

$$\Psi_0(I_1) = \frac{1}{2}(I_1 - 3) + \frac{1}{20N}(I_1^2 - 9) + \frac{11}{1050N^2}(I_1^3 - 27) \\ + \frac{19}{7000N^3}(I_1^4 - 81) + \frac{519}{673750N^4}(I_1^5 - 243) \tag{2.12}$$

2.2 Electric constitutive equation

The electric constitutive equation is given as,

$$\boldsymbol{d} = \epsilon_0 \ \boldsymbol{e} + \boldsymbol{p} \tag{2.13}$$

where ϵ_0 is the vacuum electric permittivity, $\boldsymbol{p}$ is the electric polarization density.

It is important to note that the first and second terms on the right-hand side of equation (2.13) give the contribution of free space and condensed matter, respectively and in vacuum $\boldsymbol{d} = \epsilon_0 \boldsymbol{e}$.

In the reference configuration, the electric displacement $\boldsymbol{D}$ is given as,

$$\boldsymbol{D} = \epsilon_0 \ J \ \boldsymbol{C}^{-1} \ \boldsymbol{E} + \boldsymbol{P} \tag{2.14}$$

where $\boldsymbol{C}$ is the right Cauchy-Green tensor given as $\boldsymbol{C} = \boldsymbol{F}^T \boldsymbol{F}$.

2.3 Balance laws

Assuming the quasi-static theory, Maxwell's equations are considered to govern the behaviour of electric fields in the absence of magnetic fields, free currents and electric charges [12] [13]. Here we consider the Gauss law of electricity, describing the electric field generation by electric charges, given in electrostatics as,

$$\nabla_{\boldsymbol{x}} \cdot \boldsymbol{d} = 0 \tag{2.15}$$

And, Faraday's law of induction, given as,

$$\nabla_{\boldsymbol{x}} \times \boldsymbol{e} = 0 \tag{2.16}$$

where $\boldsymbol{e}$ and $\boldsymbol{d}$ denote the electric field vector and electric displacement vector, respectively, in the current configuration, and $\nabla_{\boldsymbol{x}}$ is the gradient operator with respect to $\boldsymbol{x}$.

The pull-back operation of these vectors are considered to be the electric field vector and electric displacement vector in the reference configuration, given by $\boldsymbol{E}$ and $\boldsymbol{D}$, respectively where,

$$\boldsymbol{E} = \boldsymbol{F}^T \cdot \boldsymbol{e} \quad \text{and} \quad \boldsymbol{D} = J\boldsymbol{F}^{-1} \cdot \boldsymbol{d} \tag{2.17}$$

The governing equations in the reference configuration is given as,

$$\nabla_{\boldsymbol{X}} \times \boldsymbol{E} = 0 \quad \text{and} \quad \nabla_{\boldsymbol{X}} \cdot \boldsymbol{D} = 0 \tag{2.18}$$

where $\nabla_{\boldsymbol{X}}$ is the gradient operator with respect to $\boldsymbol{X}$, $\nabla_{\boldsymbol{X}} \cdot \boldsymbol{a}$ denotes the divergence and $\nabla_{\boldsymbol{X}} \times \boldsymbol{a}$ denotes the curl.

Due to the conservative nature of the electric field vector [4], as seen in equations (2.16) and (2.18), they are expressed as gradient of a scalar electric potentials φ and ϕ, given as,

$$\boldsymbol{e} = -\nabla_{\boldsymbol{x}}\varphi \quad \text{and} \quad \boldsymbol{E} = -\nabla_{\boldsymbol{X}}\phi \tag{2.19}$$

The jump condition of the electric field vector and electric displacement vector should be satisfied at the boundary of the body.

The equilibrium equation in nonlinear electroelastcity, without taking into account the mechanical body forces, is given in the current configuration as,

$$\nabla_{\boldsymbol{x}} \cdot \boldsymbol{\sigma}^T + \boldsymbol{f}_e = 0 \tag{2.20}$$

where $\boldsymbol{\sigma}$ is the Cauchy stress tensor and $\boldsymbol{f}_e$ is the electric body force per unit volume given as,

$$\boldsymbol{f}_e = [\nabla_{\boldsymbol{x}}\boldsymbol{e}]\boldsymbol{p} \tag{2.21}$$

Using equations (2.13) and (2.21), we get

$$\boldsymbol{f}_e = \nabla_{\boldsymbol{x}} \cdot [\boldsymbol{e} \otimes \boldsymbol{d} - \frac{1}{2}\epsilon_0[\boldsymbol{e} \cdot \boldsymbol{e}]\boldsymbol{I}] \tag{2.22}$$

where $\otimes$ denotes the cross product and the second term on the right hand side corresponds to the Maxwell stress [23] [22].

Therefore, the equilibrium equation (2.20) can be written as,

$$\nabla_{\boldsymbol{x}} \cdot \boldsymbol{\tau}^T = 0 \tag{2.23}$$

where $\boldsymbol{\tau}$ is the total stress tensor defined as,

$$\boldsymbol{\tau} = \boldsymbol{\sigma} + \boldsymbol{d} \otimes \boldsymbol{e} - \frac{1}{2}\epsilon_0[\boldsymbol{e} \cdot \boldsymbol{e}]\boldsymbol{I} \tag{2.24}$$

Since the balance of angular momentum requires that,

$$\boldsymbol{\varepsilon}\boldsymbol{\tau} = 0 \tag{2.25}$$

where $\boldsymbol{\varepsilon}$ denotes the third-order permutation tensor, the total stress tensor should be symmetric and therefore the Cauchy stress tensor is, in general, non-symmetric.

To find the counterpart of total stress tensor $\boldsymbol{\tau}$ in the reference configuration, a pull-back operation [11] is performed to give a total nominal stress tensor $\boldsymbol{T}$ as,

$$\boldsymbol{T} = J\,\boldsymbol{F}^{-1}\,\boldsymbol{\tau} \tag{2.26}$$

Hence, the equilibrium equation in reference configuration is given as,

$$\nabla_{\boldsymbol{X}} \cdot \boldsymbol{T}^T = 0 \tag{2.27}$$

At the boundary of the body, the total nominal stress tensor should satisfy the jump condition, in the material configuration as,

$$\boldsymbol{N} \cdot [\![\boldsymbol{T}]\!] = 0 \tag{2.28}$$

where $\boldsymbol{N}$ is the unit normal to the surface and $[\![\cdot]\!]$ denotes the jump.

The equations (2.23) and (2.27) gives the Eulerian and Lagrangian formulation of the governing equations of nonlinear electroelastic problem, which can be solved using either of the formulations.

Chapter 3

Finite Element Method

One of the most utilised numerical method for solving problems in computational mechanics is the Finite Element Method (FEM) [16] [13] [3] [11] [4] [12]. The method is used to obtain approximate solution of a boundary value problem at discrete number of points over the considered domain.

In this method, the Minimum Potential Energy (MPE) principle is used to find the stationary condition of the total potential energy consisting of the internal energy (strain energy) and external work. The system of equations resulting from the variational formulation are solved over discretized smaller subdomains known as elements and are assemble to form the global system of equations.

In order to solve these nonlinear system of equations we need to linearize the problem and solve it using the Newton-Raphson method [11]. A finite element method is described by a variational formulation, a discretization strategy and linearization. This chapter presents these major constituents of the method required to solve the nonlinear electromechanical problem.

3.1   Variational formulation

The Minimum Potential Energy (MPE) principle states that the actual displacement solution $u^*(x)$ that satisfies the governing equations is the one which renders the TPE (Total Potential Energy) functional stationary i.e.

$$\delta W = \delta W_{int} - \delta W_{ext} = 0 \quad \Longleftrightarrow \quad u = u^*$$

The variational formulation of this problem therefore requires definition of a functional whose stationary condition are the governing system of equations. The functional W is a function of

strain energy density and consists of W_{int} − internal energy density per referential unit volume, and W_{ext} − external work per referential unit volume contributions i.e.

$$W = W_{int} - W_{ext} = \int_{\Omega_0} \Psi(\boldsymbol{F}, \boldsymbol{E})dV - \int_{\partial\Omega_{0\tau}} \boldsymbol{\chi} \cdot \overline{\boldsymbol{T}}dA + \int_{\partial\Omega_{0q}} \phi\overline{Q}dA \qquad (3.1)$$

where internal and external works are defined as,

$$W_{int} = \int_{\Omega_0} \Psi(\boldsymbol{F}, \boldsymbol{E})dV \quad \text{and} \quad W_{ext} = \int_{\partial\Omega_{0\tau}} \boldsymbol{\chi} \cdot \overline{\boldsymbol{T}}dA - \int_{\partial\Omega_{0q}} \phi\overline{Q}dA \qquad (3.2)$$

As seen in the earlier chapter, the governing equations [12] [11] of this problem can be written in the reference configuration as,

$$\begin{aligned}
\nabla_{\boldsymbol{X}} \cdot \boldsymbol{D} &= 0 \quad \text{in} \quad \Omega_0 \\
\nabla_{\boldsymbol{X}} \cdot \boldsymbol{T}^T &= 0 \quad \text{in} \quad \Omega_0 \\
\boldsymbol{D} \cdot \boldsymbol{N} &= -\overline{Q} \quad \text{on} \quad \partial\Omega_{0q} \\
\boldsymbol{N} \cdot \boldsymbol{T} &= \overline{\boldsymbol{T}} \quad \text{on} \quad \partial\Omega_{0\tau}
\end{aligned} \qquad (3.3)$$

where $\overline{Q}$ and $\overline{\boldsymbol{T}}$ are the external electric charge and traction vector at the boundary of the considered body in the reference configuration, respectively.

Using variational calculus we can write [3],

$$\delta W = \int_{\Omega_0} \partial_{\boldsymbol{F}}\Psi : \delta\boldsymbol{F}dV + \int_{\Omega_0} \partial_{\boldsymbol{E}}\Psi \cdot \delta\boldsymbol{E}dV - \int_{\partial\Omega_{0\tau}} \delta\boldsymbol{\chi} \cdot \overline{\boldsymbol{T}}dA + \int_{\partial\Omega_{0q}} \delta\phi\overline{Q}dA \qquad (3.4)$$

Taking advantage of the dependence of strain energy function, $\Psi(\boldsymbol{F}, \boldsymbol{E})$ on the deformation gradient, $\boldsymbol{F}$ and electric field vector, $\boldsymbol{E}$ in the reference configuration and referring to equation (2.9) we have,

$$\boldsymbol{T} = [\partial_{\boldsymbol{F}}\Psi]^T \quad \text{and} \quad \boldsymbol{D} = -\partial_{\boldsymbol{E}}\Psi$$

Using this in our formulation [12], we get,

$$\delta W = \int_{\Omega_0} \boldsymbol{T}^T : \nabla_{\boldsymbol{X}} \delta \boldsymbol{\chi} dV - \int_{\Omega_0} \boldsymbol{D} \cdot (\nabla_{\boldsymbol{X}} \delta \phi) dV - \int_{\partial\Omega_{0\tau}} \delta \boldsymbol{\chi} \cdot \overline{\boldsymbol{T}} dA + \int_{\partial\Omega_{0q}} \delta \phi \overline{Q} dA \qquad (3.5)$$

Next, the use of Gauss theorem leads us to the variational formulation of the problem [3],

$$\delta W = \int_{\Omega_0} \Big[-\delta \boldsymbol{\chi} \cdot [\nabla_{\boldsymbol{X}} \cdot \boldsymbol{T}^T] + \delta \phi [\nabla_{\boldsymbol{X}} \cdot \boldsymbol{D}] \Big] dV + \int_{\partial\Omega_{0\tau}} \delta \boldsymbol{\chi} \cdot [\boldsymbol{N} \cdot \boldsymbol{T} - \overline{\boldsymbol{T}}] dA - \int_{\partial\Omega_{0q}} \delta \phi [\boldsymbol{D} \cdot \boldsymbol{N} - \overline{Q}] dA$$
$$(3.6)$$

The stationary condition $\delta W = 0$ gives us the system of equations. In order to solve this, we need to discretize the problem into smaller problems i.e. solving the system of equations over a finite number of elements and then assembling them to get the results over the whole domain.

3.2   Discretization

In the discretization method, on considering the external virtual work doesn't change, we express the internal work in reference configuration [3] as,

$$\delta W_{int} = \int_{\Omega_0} [\partial_{\boldsymbol{F}} \Psi : \delta \boldsymbol{F} + \partial_{\boldsymbol{E}} \Psi \cdot \delta \boldsymbol{E}] dV$$

On using the properties, $dV = J^{-1} dv$, $\delta \boldsymbol{F} = \nabla_{\boldsymbol{x}} \delta \boldsymbol{\chi} \cdot \boldsymbol{F}$ and $\delta \boldsymbol{E} = -\nabla_{\boldsymbol{x}} \delta \varphi \cdot \boldsymbol{F}$ [11], we can write the above internal work in current configuration as,

$$\delta W_{int} = \int_{\Omega} \Big[[J^{-1} \partial_{\boldsymbol{F}} \Psi \cdot \boldsymbol{F}^T] : \nabla_{\boldsymbol{x}} \delta \boldsymbol{\chi} - [J^{-1} \partial_{\boldsymbol{E}} \Psi \cdot \boldsymbol{F}^T] \cdot \nabla_{\boldsymbol{x}} \delta \varphi \Big] dv \qquad (3.7)$$

Now noting that in the current configuration, the total stress tensor, $\boldsymbol{\tau}^T$, the Eulerian counterpart of $\boldsymbol{T}^T$, is given as,

$$\boldsymbol{\tau}^T = J^{-1} \partial_{\boldsymbol{F}} \Psi \cdot \boldsymbol{F}^T \quad \text{or} \quad \boldsymbol{\tau} = J^{-1} \boldsymbol{F} \cdot \boldsymbol{T}$$

and electric displacement in current configuration is given as,

$$\boldsymbol{d} = -J^{-1}\partial_{\boldsymbol{E}}\Psi \cdot \boldsymbol{F}^T$$

Here, we use the finite element discretization process [4] to get,

$$\delta W_{int} = \sum_{e=1}^{nel} \sum_{k=1}^{nen} \delta\boldsymbol{\chi}_k \cdot \int_{\Omega^e} \boldsymbol{\tau}^T \cdot \nabla_{\boldsymbol{x}} N^k dv + \delta\varphi_k \int_{\Omega^e} \boldsymbol{d} \cdot \nabla_{\boldsymbol{x}} N^k dv \tag{3.8}$$

where, N^k are the usual shape functions [11] of finite element e at node k. nel and nen are the number of elements and the number of nodes per element, respectively. Also, φ_k and $\boldsymbol{\chi}_k$ are the electric potential and displacement vector at node k.

Hence, now the condition $\delta W_{int} = 0$ is a nonlinear system of equations with unknowns $\boldsymbol{\chi}$ and φ.

3.3 Linearization

We use the Newton-Raphson method [11] to solve the nonlinear system of equations by first making it linearized i.e. $\delta W + \Delta\delta W = 0$.

This gives us,

$$\begin{aligned}
\delta W + \Delta\delta W = \delta \int_{\Omega_0} \Psi dV + \int_{\Omega_0} \Big(&\delta\boldsymbol{F} : \partial^2_{\boldsymbol{F}\boldsymbol{F}}\Psi : \Delta\boldsymbol{F} + \delta\boldsymbol{F} : \partial^2_{\boldsymbol{F}\boldsymbol{E}}\Psi \cdot \Delta\boldsymbol{E} \\
&+ \delta\boldsymbol{E} \cdot \partial^2_{\boldsymbol{E}\boldsymbol{F}}\Psi : \Delta\boldsymbol{F} + \delta\boldsymbol{E} \cdot \partial^2_{\boldsymbol{E}\boldsymbol{E}}\Psi \cdot \Delta\boldsymbol{E} \Big) dV
\end{aligned} \tag{3.9}$$

Again we write $\Delta\delta W$ in current configuration as [12] [3],

$$\begin{aligned}
\Delta\delta W = \int_{\Omega} \Big[&\nabla_{\boldsymbol{x}}\delta\boldsymbol{\chi} : \underline{\boldsymbol{b}} : \nabla_{\boldsymbol{x}}\Delta\boldsymbol{\chi} - \nabla_{\boldsymbol{x}}\delta\boldsymbol{\chi} : \underline{\boldsymbol{D}} \cdot \nabla_{\boldsymbol{x}}\Delta\varphi \\
&- \nabla_{\boldsymbol{x}}\delta\varphi \cdot \underline{\boldsymbol{D}}^T : \nabla_{\boldsymbol{x}}\Delta\boldsymbol{\chi} + \nabla_{\boldsymbol{x}}\delta\varphi \cdot \underline{\boldsymbol{E}} \cdot \nabla_{\boldsymbol{x}}\Delta\delta\varphi \Big] dv
\end{aligned} \tag{3.10}$$

where,

$$\underline{\boldsymbol{b}} = J^{-1}[\boldsymbol{I}\overline{\otimes}\boldsymbol{F}] : \partial^2_{\boldsymbol{FF}}\Psi : [\boldsymbol{I}\overline{\otimes}\boldsymbol{F}^T]$$

$$\underline{\boldsymbol{D}} = J^{-1}[\boldsymbol{I}\overline{\otimes}\boldsymbol{F}] : \partial^2_{\boldsymbol{FE}}\Psi \cdot \boldsymbol{F}^T$$

$$\underline{\boldsymbol{E}} = J^{-1}\boldsymbol{F} \cdot \partial^2_{\boldsymbol{EE}}\Psi \cdot \boldsymbol{F}^T$$

$$(A\overline{\otimes}B)_{ijkl} = A_{ik}B_{jl}$$

Thus discretizing with finite elements [12], we get,

$$
\begin{aligned}
\Delta\delta W = \sum_{e=1}^{nel}\sum_{k,l=1}^{nen}\int_{\Omega^e} &\Big([\delta\boldsymbol{\chi}_k \otimes \nabla_{\boldsymbol{x}}N^k] : \underline{\boldsymbol{b}} : [\Delta\boldsymbol{\chi}_l \otimes \nabla_{\boldsymbol{x}}N^l] \\
&- [\delta\boldsymbol{\chi}_k \otimes \nabla_{\boldsymbol{x}}N^k] : \underline{\boldsymbol{D}} \cdot [\Delta\varphi_l\nabla_{\boldsymbol{x}}N^l] \\
&- [\delta\varphi_k\nabla_{\boldsymbol{x}}N^k] \cdot \underline{\boldsymbol{D}}^T : [\Delta\boldsymbol{\chi}_l \otimes \nabla_{\boldsymbol{x}}N^l] \\
&+ [\delta\varphi_k\nabla_{\boldsymbol{x}}N^k] \cdot \underline{\boldsymbol{E}} \cdot [\Delta\varphi_l\nabla_{\boldsymbol{x}}N^l]\Big)dv
\end{aligned}
\tag{3.11}
$$

Now, if the component of $\boldsymbol{K}$ relating node k to node l in element (e) is given as [12],

$$[\boldsymbol{K}_{b,kl}]_{im}^e = \int_{\Omega^e}[\frac{\partial N^k}{\partial x_j}b_{ijmn}\frac{\partial N^l}{\partial x_n}]dv$$

$$[\boldsymbol{K}_{D,kl}]_i^e = -\int_{\Omega^e}[\frac{\partial N^k}{\partial x_j}\underline{D}_{ijm}\frac{\partial N^l}{\partial x_m}]dv$$

$$[\boldsymbol{K}_{E,kl}]^e = \int_{\Omega^e}[\frac{\partial N^k}{\partial x_i}\underline{E}_{ij}\frac{\partial N^l}{\partial x_j}]dv$$

we get the system of equations as [3],

$$
\begin{bmatrix} \boldsymbol{K}_b & \boldsymbol{K}_D \\ \boldsymbol{K}_D^T & \boldsymbol{K}_E \end{bmatrix}
\begin{Bmatrix} \Delta\boldsymbol{\chi} \\ \Delta\varphi \end{Bmatrix} =
\begin{Bmatrix} \boldsymbol{f}_\tau \\ \boldsymbol{f}_q \end{Bmatrix}
\tag{3.12}
$$

where, the element contribution to the right hand side is,

$$\boldsymbol{f}_\tau^e = - \int_{\Omega^e} \boldsymbol{\tau}^T \cdot \nabla_{\boldsymbol{x}} N^k dv + \int_{\partial\Omega_\tau^e} N^k \bar{\boldsymbol{t}} da$$

$$\boldsymbol{f}_q^e = - \int_{\Omega^e} \boldsymbol{d} \cdot \nabla_{\boldsymbol{x}} N^k dv + \int_{\partial\Omega_q^e} N^k \bar{q} da$$

The Newton Raphson algorithm [11] used in the Matlab implementation is shown in Table 3.1. A line-search algorithm is implemented to be used in combination with Newton Raphson method.

Newton Raphson algorithm
INPUT geometry, material properties & solution parameters
INITIALIZE $F = 0, x = X$ (initial geometry), $R = 0$
FIND initial K (tangent stiffness matrix)
LOOP over load increments
FIND $\varDelta$F (the load increment)
SET F = F +$\varDelta$F
SET R = R -$\varDelta$F
DO WHILE (||R|| / ||F|| > tolerance)
SOLVE K u = -R
UPDATE x = x + u
FIND T and K
FIND R = T - F
END DO
END LOOP

TABLE 3.1: Newton Raphson algorithm.

Line search is an optimization tool that helps in identifying the minimum energy of the system by adding stability to the solution and thus leading to a better solution. In the line-search strategy, the algorithm chooses a search direction s_k and tries to solve the following 1D minimization problem

$$\min_{t>0} f(x_k + ts_k)$$

where the scalar t is the step-length. The descent direction obtained is utilised to provide stability while solving the system of nonlinear equations when the Newton-Raphson method

provides unstable (maximum energy) solution. This can be done by using the built-in Matlab function `fminbnd` or by using a backtracking method. In this research work, all numerical examples were performed using Newton-Raphson method combined with line search algorithm.

The numerical implementation was tested for the Neo-Hookean and Arruda-Boyce material models. It was evident from the results that in the case without line search, the simulation produces unstable, insignificant results and diverges, while in the other case, due to the stability provided by line search, we were able to capture the behaviour of the model [30].

Chapter 4

Numerical study and validation

4.1   A long cylinder under electric potential loading

In the first numerical study, we analyse the behaviour of a long cylinder under electric potential loading. Assuming that the cylinder is sufficiently long to have a state of plane strain along the axial direction. We consider a long cylinder with internal radius, $a = 10\ mm$ and external radius, $b = 20\ mm$. Taking advantage of the symmetry of the problem we analyse a quarter model of the 2D plane strain cylinder as shown in Figure 4.1.
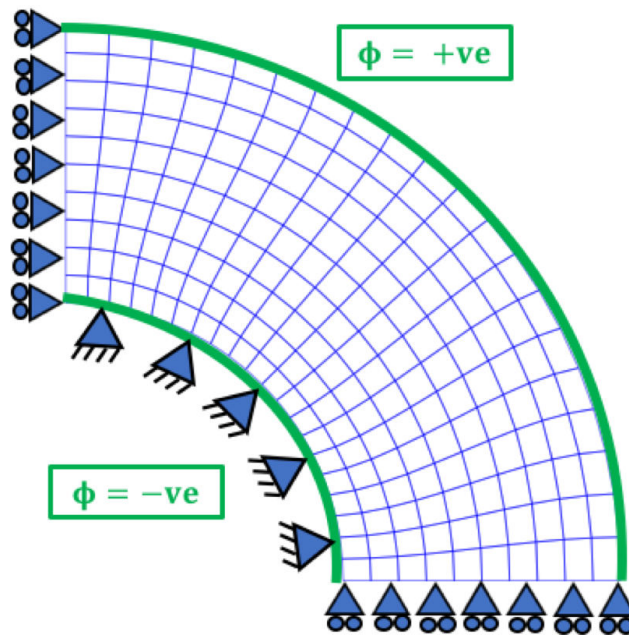
FIGURE 4.1: Model setup: A long cylinder under electric potential loading

To perform a 2D plane strain analysis of the cylinder's response (contraction) under electric potential loading, we also assume that during the deformation process, the cylinder maintains its circular symmetry with displacement as a function of radius only.

In this study, the boundary conditions are prescribed by setting the internal wall displacement to zero and the external wall displacement is let free with application of electric potential at both walls, $\phi_a = -5\ V$ and $\phi_b = +5\ V$ to develop a potential difference, $\Delta\phi = 10\ V$.

4.1.1 Pre-processing

The preprocessing software GiD was used for generating all the meshes used in this analysis. GiD has been developed by the International Center for Numerical Methods in Engineering (CIMNE) [15] and provides a complete set of tools for quick geometry definition and edition. It serves as a universal, adaptive and user-friendly pre and post processor for numerical simulations in science and engineering.

To extract the mesh data from the GiD mesh file, we use the problem type MAT-fem which is a computer program designed for introducing users to the practical use of the Finite Element Method (FEM) for analysis of structures and field problems governed by the Poisson and Laplace equations (heat transfer, acoustics, seepage, electromagnetics, etc.). Mat-fem is written in Matlab and has a user-friendly graphical user interface with the GiD pre-postprocessor [16].
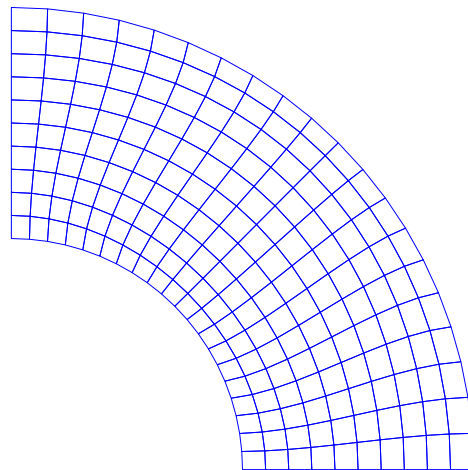

FIGURE 4.2: Mesh of 200 4-noded bilinear quadrilateral elements.

Taking advantage of the symmetry of the geometry and problem, it was decided to consider a quarter model of the long cylinder. In the 2D plain strain simulation, we start with using a mesh of 200 4-noded bilinear quadrilateral elements as shown in Figure 4.2.

We considered a strain energy density function for a Neo-Hookean like material [11] [13] [12] given as,

$$\Psi = \frac{\mu}{2}[\boldsymbol{C} : \boldsymbol{I} - 3] - \mu \ln J + \frac{\lambda}{2}[\ln J]^2 + c_1 \boldsymbol{I} : [\boldsymbol{E} \otimes \boldsymbol{E}] + c_2 \boldsymbol{C} : [\boldsymbol{E} \otimes \boldsymbol{E}]$$
$$-\frac{1}{2}\varepsilon_0 J \boldsymbol{C}^{-1} : [\boldsymbol{E} \otimes \boldsymbol{E}] \tag{4.1}$$

In order to validate [12] our implementation, we assume the values of the material constants for this example, from the previous numerical results, as $c_1 = 10 \; Pa \; m^2/V^2$ and $c_2 = 6 \; Pa \; m^2/V^2$. For this study we also assume the following material properties, bulk modulus, $\kappa = 10 \; MPa$, shear modulus, $\mu = 5 \; MPa$ and the parameter $\lambda = \kappa - 2\mu/3 = 6.667 \; MPa$.

Since it is difficult to determine an analytical result for our problem, we analyse our implementation results with a reference solution. The result obtained from this comparison gives us an option to evaluate the finite element method developed in Matlab and validate our results with the numerical results of 'FEM 2D Plain Strain Case 3' by Vu et al. [12].

Using the property that the nominal stress tensor, $\boldsymbol{T} = [\partial_{\boldsymbol{F}} \Psi]^T$ and the electric displacement vector, $\boldsymbol{D} = -\partial_{\boldsymbol{E}} \Psi$, we have [12],

$$\boldsymbol{T} = \left[\mu \boldsymbol{F} - \mu \boldsymbol{F}^{-T} + \lambda \ln J \boldsymbol{F}^{-T} + 2c_2 \boldsymbol{F} \cdot [\boldsymbol{E} \otimes \boldsymbol{E}] \right]^T \tag{4.2}$$

$$\boldsymbol{D} = -2c_1 \boldsymbol{E} - 2c_2 \boldsymbol{C} \cdot \boldsymbol{E} \tag{4.3}$$

Also, in order to calculate $\underline{\boldsymbol{b}}$, $\underline{\boldsymbol{D}}$ and $\underline{\boldsymbol{E}}$, we need to derive the following expressions [3],

$$[\partial^2_{\boldsymbol{F}\boldsymbol{F}} \Psi]_{mnpq} = \mu \delta_{mp} \delta_{nq} + [\mu - \lambda \ln J] F^{-1}_{np} F^{-1}_{qm} + \lambda F^{-1}_{nm} F^{-1}_{qp} + 2c_2 \delta_{mp} E_q E_n \tag{4.4}$$

$$[\partial^2_{\boldsymbol{FE}}\Psi]_{mnp} = 2c_2[F_{mi}E_i\delta_{np} + F_{mp}E_n] \tag{4.5}$$

$$[\partial^2_{\boldsymbol{EE}}\Psi]_{mn} = 2c_1\delta_{mn} + 2c_2C_{mn} \tag{4.6}$$

$$\frac{\partial C^{-1}_{ij}}{\partial F_{mn}} = -(C^{-1}_{ik}C^{-1}_{jn} + C^{-1}_{in}C^{-1}_{jk})F_{mk} \tag{4.7}$$

4.1.2 Results and validation

The solutions obtained from the implementation are shown in Figures 4.3 and 4.4. On application of electric potential difference, $\Delta\phi = 10\ V$, the contraction of the cylindrical pipe as well as the distribution of the electric potential through the thickness of the cylinder can be seen in Figure 4.3, where the colour legend depicts the electric potential.
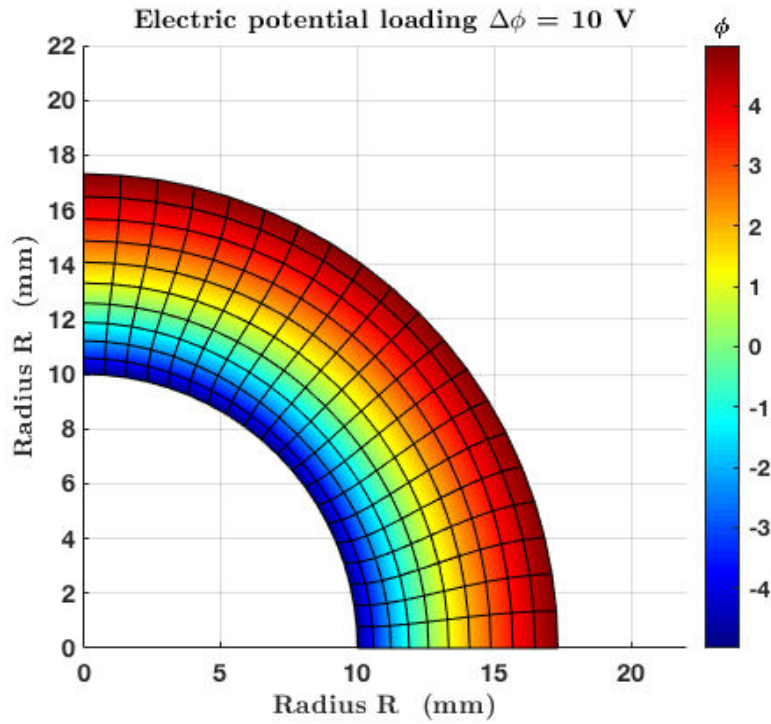
FIGURE 4.3: Contraction of a long cylinder under electric potential loading of $\Delta\phi = 10\ V$.

In order to understand the contraction process a little better, Figure 4.4 shows the deformation of the 2D finite element mesh used in the analysis. Here, the blue mesh refers to the reference state (undeformed) and the red mesh shows the deformation under the electric potential loading of $\Delta\phi = 10\ V$.
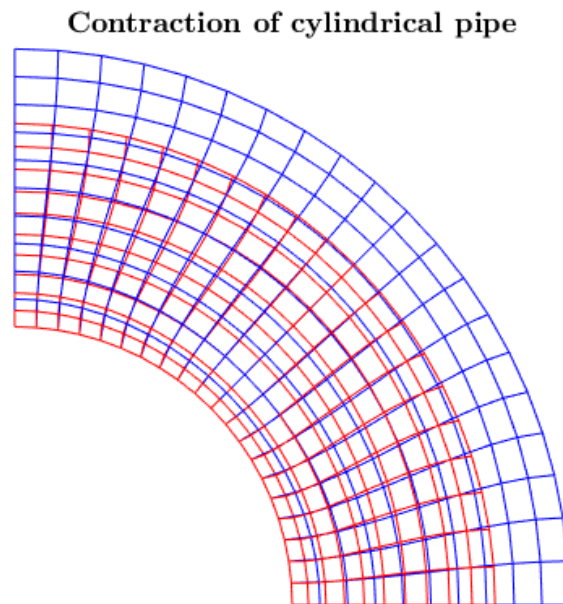
FIGURE 4.4: Deformation of the 2D finite element mesh

A comparison between the numerically obtained results and the reference results ([12]) is performed to check the correctness of our finite element implementation. As seen clearly in Figures 4.5 and 4.6, the results agree very well with the published solutions by D.K. Vu, P. Steinmann, G. Possart [12] and therefore our implementation in MATLAB is successfully validated.
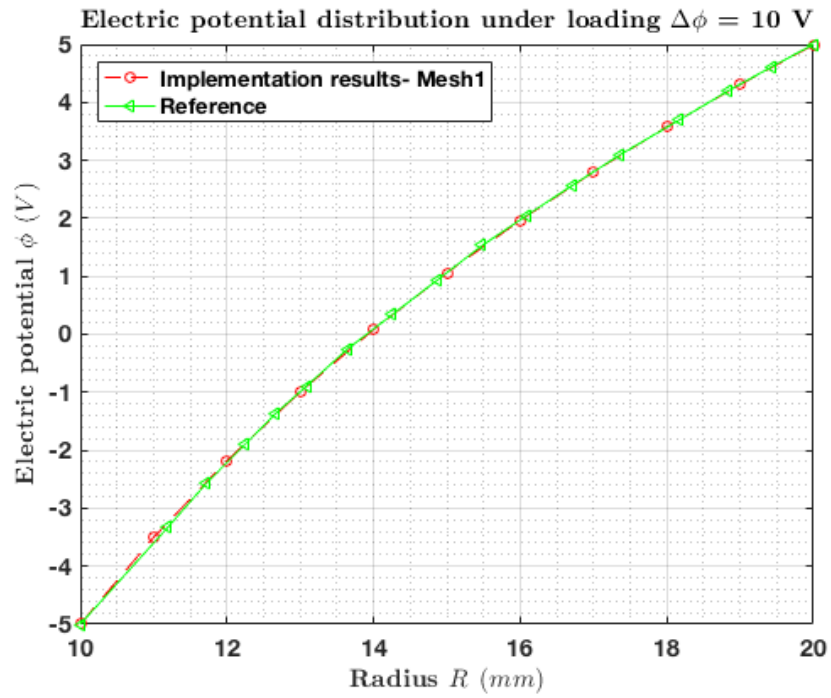
FIGURE 4.5: Comparison of numerical results for electric potential distribution under electric potential loading of $\Delta\phi = 10\ V$ with Reference (Vu et al.) [12]
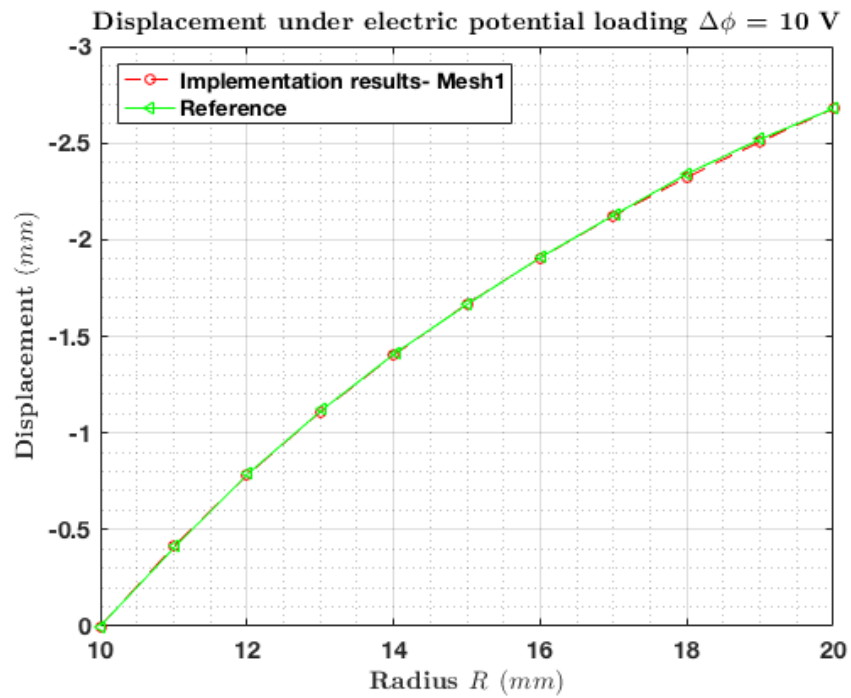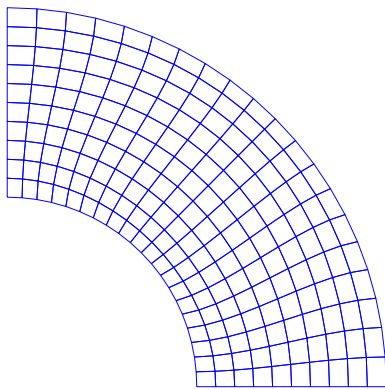

FIGURE 4.6: Comparison of numerical results for displacement under electric potential loading of $\Delta\phi = 10\ V$ with Reference (Vu et al.) [12]
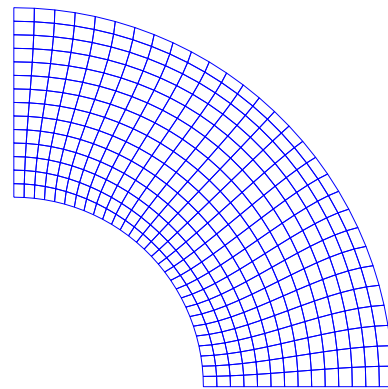
4.1.3 Grid Independence Study (GIS)

Carrying out grid independence test is vital in determining the precision of numerical implementation. The idea behind this study is to perform the analysis with subsequent smaller mesh sizes and check if the results obtained are within a small tolerance. Essentially, it gives us option to use a coarser mesh (converged) to simulate the behaviour of the model with little approximation and low computational cost.
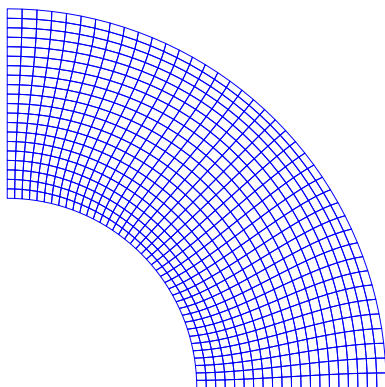
In this research work, four mesh sizes as shown in Figure 4.7 were studied for the long cylinder model, with number of elements varying from 200 to 1593.
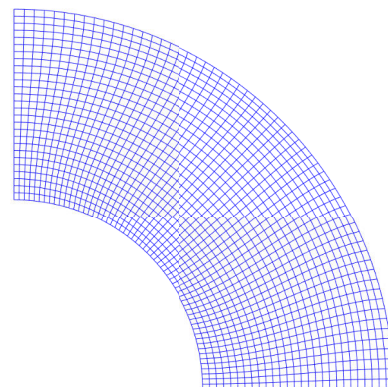

(a) Mesh1: 200 elements

(b) Mesh2: 406 elements

(c) Mesh3: 800 elements

(d) Mesh4: 1593 elements

FIGURE 4.7: Meshes used in the grid independence study.

Figures 4.8 and 4.9 show the results obtained for the different meshes and the reference solution. A comparison of the displacement and electric potential distribution across the radius of the long cylinder for different mesh sizes is presented.
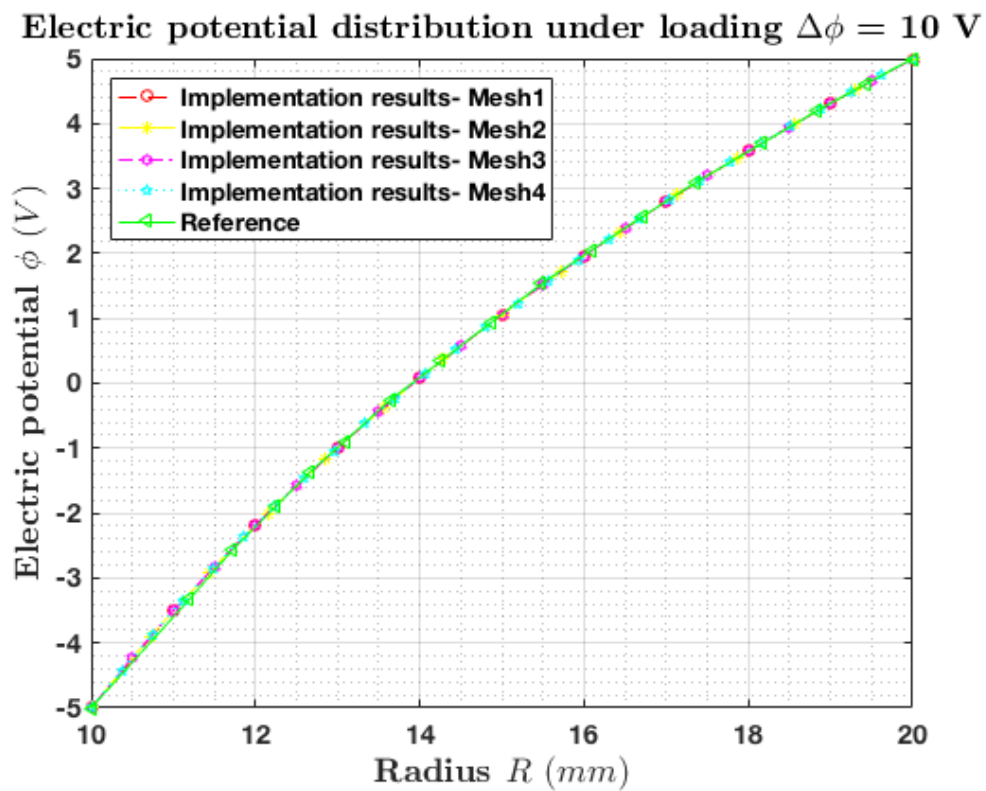

FIGURE 4.8: GIS - Electric potential distribution under electric potential loading of $\Delta\phi =$ 10 V compared with the Reference (Vu et al.) [12]
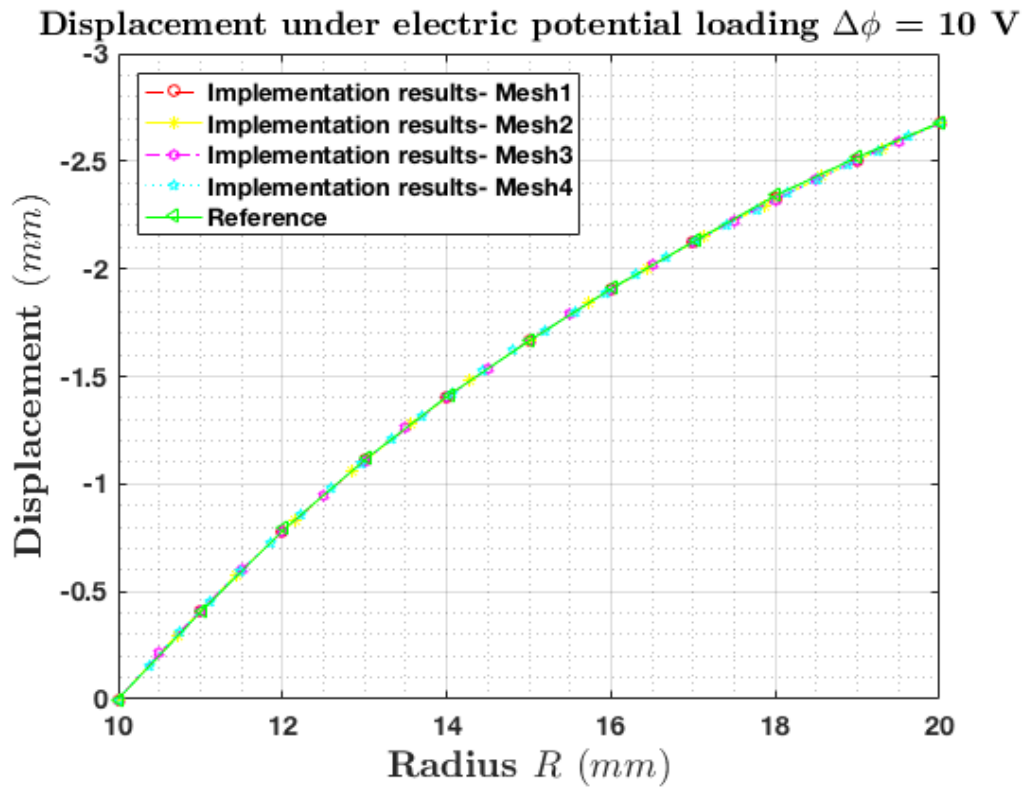
FIGURE 4.9: GIS - Displacement under electric potential loading of $\Delta\phi = 10\ V$ compared with the Reference (Vu et al.) [12]

We can easily deduce from the figures that the all meshes show similar trend with minimal difference between the results obtained. Therefore, it is inferred that the initial mesh, Mesh1 used in the analysis is mesh independent. Therefore based on this Grid Independence Study, it was decided to use this mesh as a standard mesh for further analysis.

4.2   A thin elastomeric film under electric potential load

In this numerical study, we analyse a thin elastomeric film under electric potential loading of $\Delta\phi = 10\ V$ as shown in Figure 4.10.
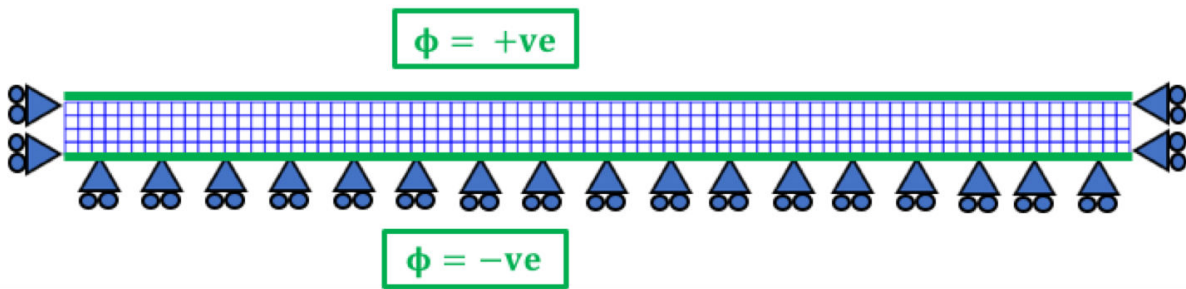

FIGURE 4.10: Model setup: A thin elastomeric film under electric potential load

The 2D film model used in the analysis is of the dimensions, $4\ mm \times 80\ mm$. The film is modelled as a compressible dielectric in order to compare with the results obtained for an incompressible or nearly incompressible dielectric elastomer.

The boundary conditions are prescribed by setting the inner and side boundary displacement to zero and the outer boundary displacement is let free.

4.2.1   Pre-processing

The preprocessing software GiD was used for generating the mesh shown in Figure 4.11. To extract the mesh data from the GiD mesh file, we use the problem type MAT-fem with graphical user interface of GiD pre-postprocessor.

FIGURE 4.11: Mesh of 320 4-noded bilinear quadrilateral elements

In this study, we used the Arruda-Boyce strain energy density function [13] to model the mechanical behaviour of the dielectric elastomer. It is given as,

$$\Psi(\boldsymbol{C}, \boldsymbol{E}) = \mu\Psi_0 - 2\mu\Psi_0\ln J - \frac{\lambda}{2}[\ln J]^2 + c_1\boldsymbol{I} : [\boldsymbol{E} \otimes \boldsymbol{E}] + c_2\boldsymbol{C} : [\boldsymbol{E} \otimes \boldsymbol{E}] \tag{4.8}$$

where we neglect the contribution of free space term $(1/2\varepsilon_0\boldsymbol{C}^{-1} : [\boldsymbol{E} \otimes \boldsymbol{E}])$ and the mechanical free energy, Ψ_0 is approximated by a truncated series expansion.

4.2.2 Results and discussion

The solutions obtained from the implementation are shown in Figures 5.7 and 4.13. On application of electric potential difference, $\Delta\phi = 10\ V$, the contraction of the elastomeric film as well as the distribution of the electric potential through the thickness of the film can be seen in Figure 5.7, where the colour legend depicts the electric potential.

The contraction process can be seen in Figure 4.13 where the deformation of the 2D finite element mesh used in the analysis is plotted. Here, the blue mesh refers to the reference state (undeformed) and the red mesh shows the deformation under the electric potential loading of $\Delta\phi = 10\ V$.
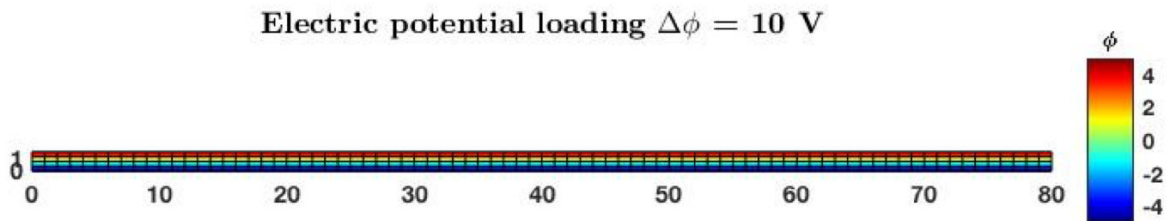
FIGURE 4.12: Contraction of a thin compressible elastomeric film under electric potential loading of $\Delta\phi = 10\ V$
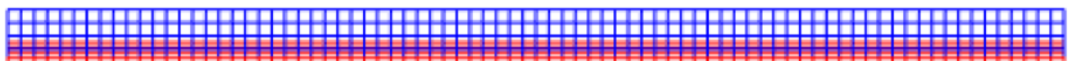

FIGURE 4.13: Deformation of the 2D finite element mesh of thin compressible elastomeric film

Chapter 5

Incompressible DE

While modelling an incompressible or nearly incompressible dielectric elastomer film, we encounter volumetric locking as shown in Figure 5.1. Mesh locking is usually confronted in Finite Element Method while working with incompressible materials [4]. As the Poisson's ratio approaches 0.5, Lamé's parameter λ becomes very large predicting excessive stiffness and generating erroneous results. The bilinear quadrilateral used while modelling compressible film in Chapter 4 are susceptible to locking [29]. The typical overly stiff behaviour of the film can be observed in Figure 5.1.
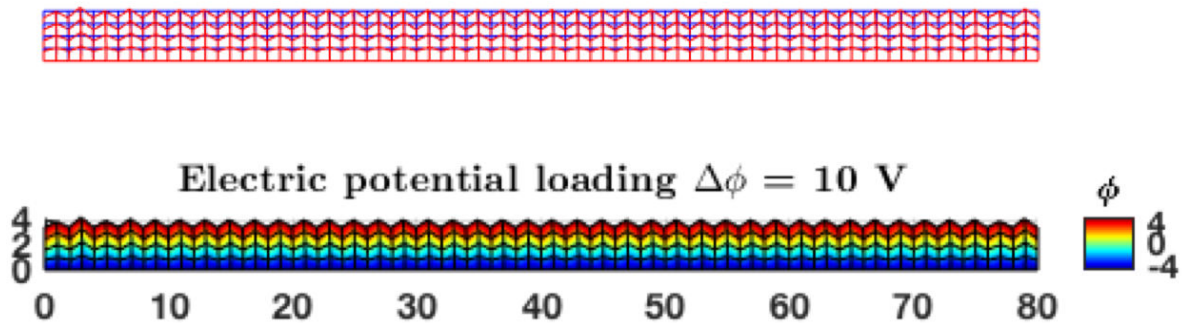

FIGURE 5.1: Instabilities due to mesh locking

Various techniques to prevent this locking have been proposed in the literature like the choice of element type [29] and reduced integration [11]. In this work, we choose a different element type, a diamond mesh [29], in order to combat this locking.

Diamond meshes are conformal meshes derived from conventional triangular elements. Hauret, Kuhl and Ortiz [29] evaluated the performance of different lower order elements compared

36

to variants of two-dimensional diamond elements and predicted that diamond element 2P1P0 (shown in Figure 5.2) has optimal convergence and stability properties.
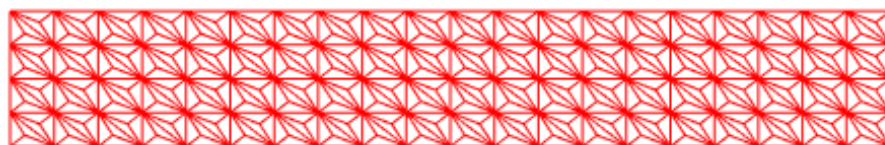

FIGURE 5.2: Diamond mesh elements used for the film.

The simulation and geometric parameters are kept same in this problem, where the nearly incompressible dielectric elastomeric film of 80 $mm \times$ 4 mm is constrained at the bottom and the sides.

A potential difference is applied along the thickness of the film. As expected, with the application of electric potential, there is a little deformation of the film as shown in Figure 5.3.

It is intuitive to assume that introducing extra nodes will increase the problem's complexity. However, improved interpolation in case of diamond meshes results in less computational cost [29].
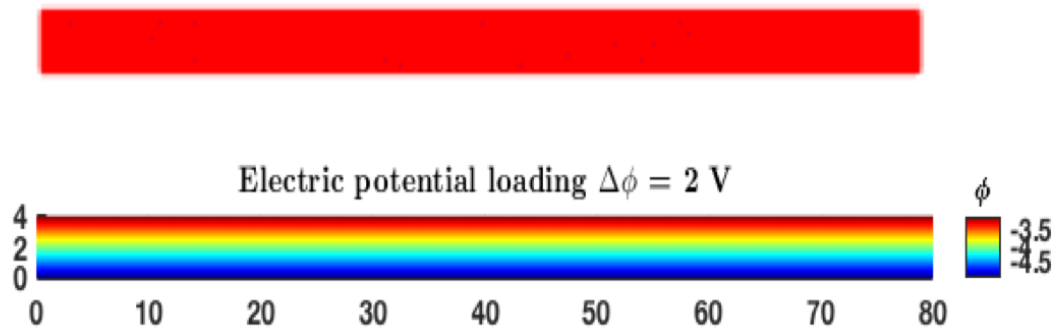
FIGURE 5.3: Behaviour of nearly incompressible elastomeric film on application of electric potential across the thickness with a mesh of 320 elements.
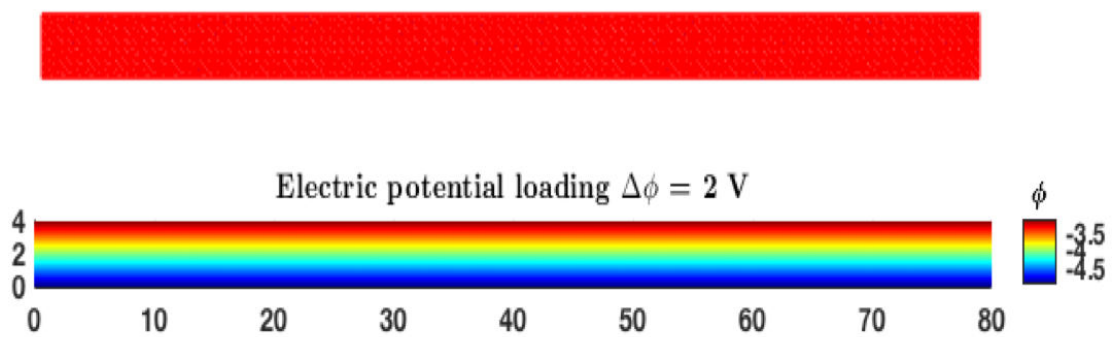

FIGURE 5.4: Behaviour of nearly incompressible elastomeric film on application of electric potential across the thickness with a mesh of 600 elements.

5.1   Instabilities

Description of the instabilities associated with dielectric elastomeric actuators is vital in understanding the application areas of a DEA. It has been shown in the literature that surface tension can have a significant impact [13] on the deformation of these materials and therefore could be utilised to deform the material in controllable and unique ways.

The effect of surface tension on the deformation of a dielectric elastomer has been studied recently for applications in energy harvesting, artificial muscles and flexible electronics [13]. A major contribution in the theoretical and experimental results for dielectric electroelastic instabilities has been made by the works of Zhao and Wang [18] [19] [14].

5.1.1   Surface tension

The elastocapillary forces exerted by fluids at rest on a solid has been studied to harness the controllable deformation using elastocapillary forces or surface tension. The control comes through the elastocapillary number defined as $\gamma/\mu l$, where γ is the surface tension, μ is the shear modulus, and l is the characteristic length.

While the elastocapillary effect on soft materials has been studied extensively, the instability associated with this effect is still under research. The experimental work by Wang and Zhao [14] showed the dependence of surface tension on the instability mechanism and Seifi and Park [13] investigated the electro-elastocapillary effect computationally.

In this work, the surface tension effect is incorporated in the developed finite element model for finite deformation in dielectric elastomers with an aim to capture the instabilities where surface tension interacts with the electromechanical transduction. A few instabilities studied recently are the snap-through [13], surface creasing and wrinkling [14], and bursting drops [19]. The developed model is used to simulate the effect of surface creasing and wrinkling and analyse its dependence on surface tension and elastocapillary number $\gamma/(\mu H)$.

The material incompressibility in the film model, previously used in the simulations in Chapter 4, is enforced by assuming a high value of bulk modulus, κ, compared to the shear modulus, μ.

It is also shown by Park et al. [13] that incorporating the surface tension in the electroelasticity model leads us to two new terms, the surface stiffness $\boldsymbol{K}_{surf}$ and the surface forces $\boldsymbol{f}_{surf}$.
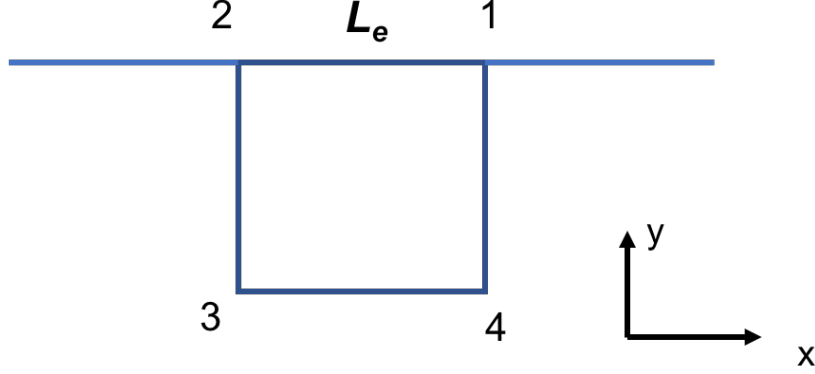

FIGURE 5.5: A finite element with the face under surface tension given by nodes 1 and 2.

Analytical derivation in the literature [26] suggests the definition of the surface forces and stiffness for a 2D element. Considering a finite element with the face under surface tension given by nodes 1 and 2, as shown in Figure 5.5, we find the length of the face as,

$$L_e = \sqrt{(x_2 - x_1)^2 + (y_2 - y_1)^2} \tag{5.1}$$

Then the surface forces and stiffness can be written as [26],

$$\boldsymbol{f}_{surf} = -\frac{h\gamma}{L_e} \begin{bmatrix} x_1 - x_2 \\ y_1 - y_2 \\ x_2 - x_1 \\ y_2 - y_1 \end{bmatrix} \tag{5.2}$$

$$\boldsymbol{K}_{surf} = \frac{h\gamma}{L_e} \begin{bmatrix} 1 & 0 & -1 & 0 \\ 0 & 1 & 0 & -1 \\ -1 & 0 & 1 & 0 \\ 0 & -1 & 0 & 1 \end{bmatrix} - \frac{h\gamma}{L_e^3} \begin{bmatrix} x_1 - x_2 \\ y_1 - y_2 \\ x_2 - x_1 \\ y_2 - y_1 \end{bmatrix} \begin{bmatrix} x_1 - x_2 \\ y_1 - y_2 \\ x_2 - x_1 \\ y_2 - y_1 \end{bmatrix}^T \tag{5.3}$$

where h is the out-of-plane thickness considered as unity [26]. These definitions of the surface forces and stiffness are then included in the coupled electroelastic system of equations as,

$$\begin{bmatrix} \boldsymbol{K}_b + \boldsymbol{K}_{surf} & \boldsymbol{K}_D \\ \boldsymbol{K}_D^T & \boldsymbol{K}_E \end{bmatrix} \begin{Bmatrix} \Delta\boldsymbol{\chi} \\ \Delta\varphi \end{Bmatrix} = \begin{Bmatrix} \boldsymbol{f}_\tau + \boldsymbol{f}_{surf} \\ \boldsymbol{f}_q \end{Bmatrix} \tag{5.4}$$

It is clearly seen that the difference in the system of equations with surface tension and the system given in equation (3.12) is the addition of the surface stiffness $\boldsymbol{K}_{surf}$ to the mechanical stiffness matrix and the corresponding force $\boldsymbol{f}_{surf}$ to the corresponding right hand side force vector.

5.1.2 Instability numerical analysis

The numerical example in this study is set up as shown in Figure 5.6. Multiple simulations are performed with varying surface tension on the outer boundary of the incompressible dielectric elastomeric film.

Other parameters in this study are kept the same as the previous cases to understand the effect of adding surface tension in electromechanical coupling. The potential difference is increased iteratively till surface instabilities are observed in the model. The simulation results for varying elastocapillary number are generated and analysed in the following section.
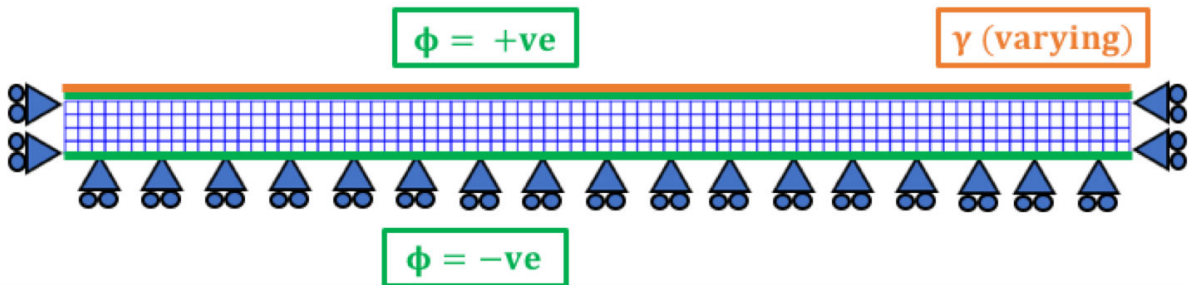

FIGURE 5.6: Model setup: A thin elastomeric film under electric potential load and surface tension on outer boundary

5.1.3 Results and discussion

The solutions obtained from the implementation, explained above, after incorporating surface tension effect are shown in Figures 5.7 - 5.10.
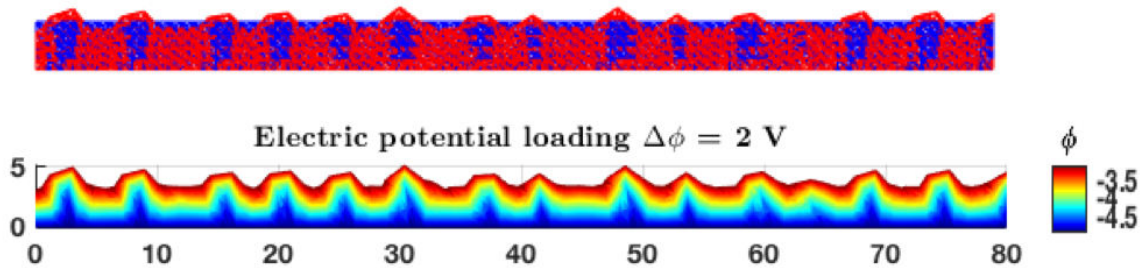

FIGURE 5.7: Instabilities due to surface tension on the top surface of the film with varying elastocapillary number $\gamma/(\mu H) \approx \mathbf{0.6}$ with a mesh of 320 elements.

The study was performed using meshes of 320 and 600 elements with iteratively application of surface tension and electric potential. The results obtained show that the elastocapillary number determines the type of instability shown by the dielectric elastomeric film.
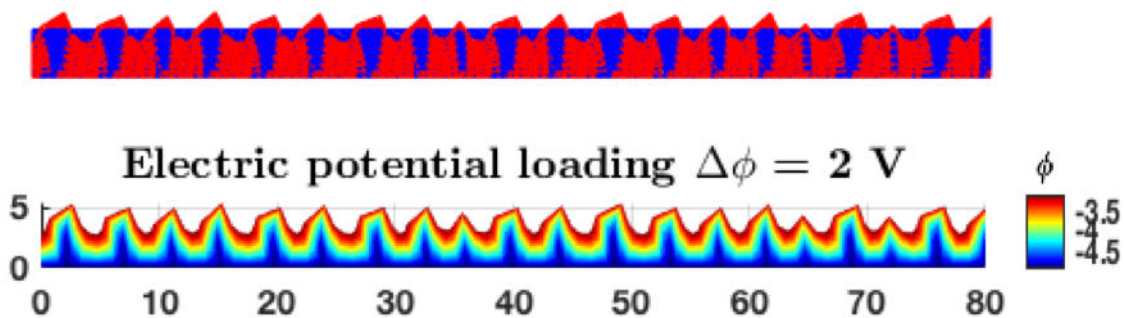

FIGURE 5.8: Instabilities due to surface tension on the top surface of the film with varying elastocapillary number $\gamma/(\mu H) \approx \mathbf{0.6}$ with a mesh of 600 elements.

Based on the experimental [18] and numerical literature [13], a change in surface instability is observed in a dielectric elastomer with varying elastocapillary number. When this factor is small, a surface instability of creasing type with short instability wavelength is observed, however with higher elastocapillary number the instability transition to wrinkling is observed which is distinguished by higher instability wavelengths.
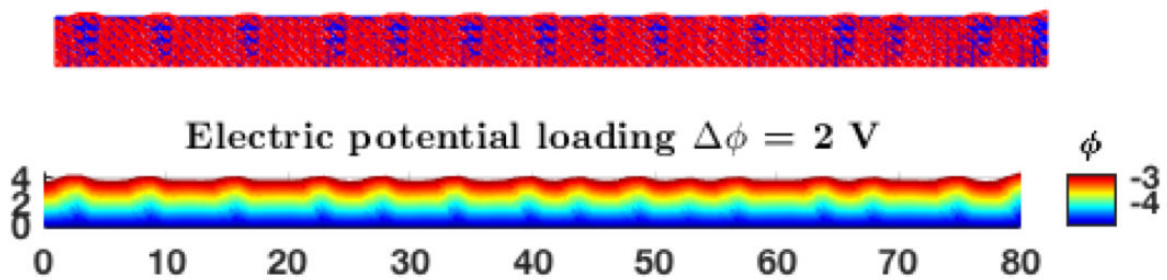

FIGURE 5.9: Instabilities due to surface tension on the top surface of the film with varying elastocapillary number $\gamma/(\mu H) \approx \mathbf{2.4}$ with a mesh of 320 elements.
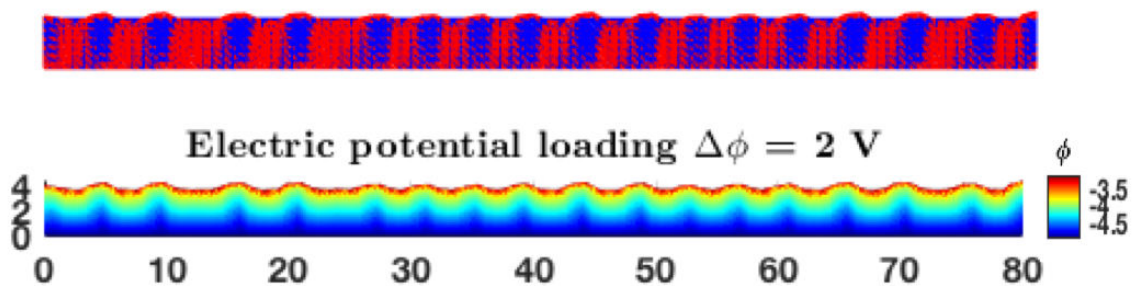

FIGURE 5.10: Instabilities due to surface tension on the top surface of the film with varying elastocapillary number $\gamma/(\mu H) \approx \mathbf{2.4}$ with a mesh of 600 elements.

As shown, we are able to capture the general trend of the surface instabilities in the elastomeric film using finite element analysis. The implementation results from MATLAB match closely with the numerical [13] and experimental [18] results for creasing effect. Although the FEM code implemented predicts a shorter wavelength in wrinkling instability than the experimental results, it has been able to capture the transition effectively with varying surface tension which could be useful in understanding the behaviour of a dielectric elastomer actuator under surface tension.

Chapter 6

Conclusions

With the exponential growth in computing power, understanding the mathematical theory of nonlinear electromechanical coupling and predicting the material's behaviour under different loading conditions, are crucial in designing and developing the future smart devices.

This research work presented the framework of electromechanical coupling and finite strain deformation for dielectric elastomer actuators applications and its implementation in MATLAB.

Using Finite Element Method, we analysed the numerical solution of boundary value problems for a long cylinder, compressible film and nearly incompressible elastomeric film, and validated with the research work published in the area of dielectric elastomeric actuators.

Since it is important to describe the instabilities associated with these soft materials, an analysis of the surface instabilities in DEs due to surface tension has been performed and the instability transition is found to be related to the elastocapillary number. It was observed that application of higher surface tension resists the deformation that would essentially occur due to applied voltage. The transition from creasing to wrinkling can be observed by analysing the increase in wavelength of the surface instability in a dielectric elastomeric film.

A lesser-known phenomenon that has recently attracted significant attention is flexoelectricity [27] [28] [7], an electrical polarisation induced by a strain gradient. Meanwhile, piezoelectric effect exists only in materials having a non-centrosymmetric crystal structure. On the other hand, flexoelectricity is free from this restriction on the crystal structure, but can only be significantly observed in materials capable of undergoing large strain gradients. This size-dependent property in both hard and soft materials would hold a significant importance in the development of new-age energy harvesting devices. Therefore, incorporating the flexoelectric effects at finite deformation could be a possible extension of the thesis work.

Bibliography

[1] Georges Akhras Smart materials and smart systems for the future Canadian Military Journal Autumn 2000.

[2] Parihar A.A., Kajal D. khandagale, Pallavi P. Jivrag Smart materials IOSR Journal of Mechanical and Civil Engineering (IOSR-JMCE) 3e-ISSN: 2278-1684,p-ISSN: 2320-334X, Volume 13, Issue 5 Ver. VI (Sep. - Oct. 2016), PP 28-32.

[3] Luis Dorfmann, Ray W. Ogden Nonlinear Theory of Electroelastic and Magnetoelastic Interactions ISBN 978-1-4614-9596-3 (eBook) DOI 10.1007/978-1-4614-9596-3 2014.

[4] Roman Poya, Antonio J. Gil, Rogelio Ortigosa, Ruben Sevilla, Javier Bonet, Wolfgang A. Wall, A curvilinear high order finite element framework for electromechanics: from linearised electro-elasticity to massively deformable dielectric elastomers, Computer Methods in Applied Mechanics and Engineering, 2017.

[5] Y. Bar-Cohen. Electroactive Polymer Actuators as Artificial Muscles - Reality, Potential and Challenges. SPIE, Bellingham, 2004.

[6] Lai, William, Characteristics of dielectric elastomers and fabrication of dielectric elastomer actuators for artificial muscle applications 2011 Graduate Theses and Dissertations. Paper 12183.

[7] Thanh D. Nguyen, Sheng Mao, Yao-Wen Yeh, Prashant K. Purohit, and Michael C. McAlpine Nanoscale flexoelectricity, Adv. Mater. 2013, 25,946-974, 2013.

[8] Chang-Hyo Hong, Hwang-Pill Kim, Byung-Yul Choi, Hyoung-Su Han, Jae Sung Son, Chang Won Ahn, Wook Jo Lead-free piezoceramics ? Where to move on? Journal of Materiomics Elsevier March 2016.

[9] Z. Suo, Theory of dielectric elastomers, Acta Mechanica Solida Sinica, vol. 23, no. 6, pp. 549-578, 2010.

[10] https://softroboticstoolkit.com/book/dielectric-elastomer-actuators

[11] Bonet, J., Gil, A., & Wood, R. (2016). Kinematics. In Nonlinear Solid Mechanics for Finite Element Analysis: Statics (pp. 96-136). Cambridge: Cambridge University Press. doi:10.1017/CBO9781316336144.005.

[12] D. K. Vu, P. Steinmann, and G. Possart Numerical modelling of non-linear electroelasticity IJNME September 2016.

[13] Saman Seifi, Harold S. Park Computational Modeling of Electro-Elasto-Capillary Phenomena in Dielectric Elastomers IJSS December 2015.

[14] Qiming Wang and Xuanhe Zhao Creasing-wrinkling transition in elastomer films under electric fields October 2013.

[15] GiD The personal pre and post processor https://www.gidhome.com/

[16] MAT-fem Learning the Finite Element Method with MATLAB and GiD http://www.cimne.com/mat-fem/

[17] Wissler M., Mazza E., Mechanical behaviour of an acrylic elastomer used in dielectric elastomer actuators. Sensors and Actuators A 134, 494-504 2007.

[18] Zhao, X. , Wang, Q., Harnessing large deformation and instabilities of soft dielectrics: theory, experiment, and application, Appl. Phys. Rev. 1, 2014.

[19] Wang, Q., Suo, Z., Zhao, X., Bursting drops in solid dielectrics caused by high voltages, Nature Communications, 2012 1157.

[20] Baughman R.H., C. Cui, et al., Carbon nanotune actuators, Science, vol. 284, 1999.

[21] Shahinpoor M., Kim K.J., Ionic polymer-metal composites: I. Fundamentals, Smart Mater. Struct., vol. 10, 2001.

[22] R. Pelrine, R. Kornbluh, Q. Pei, and J. Joseph, High-speed electrically actuated elastomers with strain greater than 100%, Science, vol. 287, pp. 836-839, 2000.

[23] Pelrine R., R. Kornbluh, J. Joseph Electrostriction of polymer dielectrics with compliant electrodes as a means of actuation, Sens. Actuators A, vol. A 64, pp. 77-85, 1998.

[24] Guggi Kofod, Peter Sommer-Larsen, Roy Kornbluh, Ron Perline Actuation Response of Polyacrylate Dielectric Elastomers Journal of Intelligent Material Systems and Structures, Vol. 14-December 2003

[25] Zhou J., Hong W., Zhao X., Zhang Z., Suo Z., Propagation of instability in dielectric elastomers. International Journal of Solids and Structures 45, 3739-3750, 2008.

[26] Henann, D.L., Bertoldi, K., Modeling of elasto-capillary phenomena. Soft Matter 10, 2014

[27] A. Abdollahi, C. Peco, D. Millan, M. Arroyo, and I. Arias, J. Appl. Phys. 116, 093502, 2014.

[28] Amir Abdollahi, Daniel Millan, Christian Peco, Marino Arroyo, and Irene Arias Revisiting pyramid compression to quantify flexoelectricity: A three-dimensional simulation study Physical review B 91, 104103, 2015.

[29] P. Hauret, E. Kuhl and M. Ortiz, Diamond elements: A finite element/discrete-mechanics approximation scheme with guaranteed optimal convergence in incompressible elasticity, Int. J. Numer. Meth. Engng; 72:253-294, 2007.

[30] Tae-Yeon Kim, Eric Puntel, Eliot Fried, Numerical study of the wrinkling of a stretched thin sheet, International Journal of Solids and Structures, Volume 49, Issue 5,Pages 771-782, 1 March 2012.